https://doi.org/10.5194/hess-2019-285
Preprint. Discussion started: 8 August 2019

Hydrology and Earth System Sciences
Discussions
Open Access

Comparing the performances of WRF QPF and PERSIANN-CCS QPEs in karst flood simulations and forecasting with a new Karst-Liuxihe model

Ji Li[1], Daoxian Yuan[1,2], Aihua Hong[3], Yongjun Jiang[1], Jiao Liu[4], Yangbo Chen[5],

[1]School of Geographical Sciences of Southwest University, Chongqing Key Laboratory of Karst Environment, Chongqing 400715, China

[2]Karst Dynamic Laboratory, Ministry of Land and Resources, Guilin 541004, China

[3]The Laboratory of Chongqing groundwater resourse utilization and environmental pr otection （Nanjiang Hydrogeological Team Under the Chongqing Geological Bureau of Geology and Minerals Exploration）, Chongqing 401121, China

[4]Chongqing Hydrology and Water Resources Bureau, Chongqing 401120, China

[5]Department of Water Resources and Environment, Sun Yat-sen University, Guangzhou 510275, China

Correspondence: Ji Li（445776649@qq.com）

Abstract

Long-term, available rainfall data are very important for karst flood simulations and forecasting. However, in karst areas, there is often a lack of effective precipitation available to build distributed hydrological models. Forecasting karst floods is highly challenging. Quantitative precipitation forecasts (QPF) and estimates (QPEs) could provide rational methods to acquire the available precipitation results for karst areas. Furthermore, coupling a physically-based hydrological model with the QPF and QPEs felicitously could largely enhance the performance and extend the lead time of floods forecasting in karst areas, the performance of coupling the Weather Research and Forecasting Quantitative Precipitation Forecast (WRF QPF) and Precipitation Estimations through Remotely Sensed Information based on the Artificial Neural Network-Cloud Classification System (PERSIANN-CCS QPEs) with a new fully distributed and physical hydrological model, the Karst-Liuxihe model in flood simulations and forecasting in karst area. This study served 2 main purposes: one purpose is to compare the performances of WRF QPF and PERSIANN-CCS QPEs for rainfall

https://doi.org/10.5194/hess-2019-285
Preprint. Discussion started: 8 August 2019

Hydrology and Earth System Sciences
Open Access
Discussions

forecasting in karst river basins. The other purpose is to test the effective feasibility and application of the karst flood simulation and forecasting by coupling the 2 weather models with a new Karst -Liuxihe model. The new Karst-Liuxihe model improved the structure of the model by adding the karst mechanism based on the Liuxihe model as follows: 1. Refine the model structure and put forward the concept of karst hydrological response units (KHRUs) in the model. The KHRU, as the smallest unit of the Karst-Liuxihe model, is defined in this paper to be suitable for karst basins; 2. Increase the calculations of water movement rules in the epikarst zone and underground river, such as the division of slow flow and rapid flow in the epikarst zone and the exchange of water flow between the karst fissures and conduit systems; thus, the convergence of the underground runoff calculation method is improved to be suitable for karst water-bearing media; and 3. Add some necessary hydrogeological parameters in the coupled model to reflect the true conditions of rainfall-runoff in the karst underlying surface. Moreover, the flood detention and peak clipping effects due to the upstream karst depressions during flooding were considered and reasonably calculated in the coupled model. The flood detention effect can affect the peak flow time error simulated in the model and make the true peak flow appear later; the flood peak clipping effect can affect the flood peak flow relative errors and the simulation errors of floods volume. The consideration of these 2 factors in the model makes the flood simulations and forecasting effects more credible. The rainfall forecasting result show that the precipitation distribution of the 2 weather models was very similar compared with the observed rainfall result. However, the precipitation amounts forecasted by WRF QPF were larger than that measured by the rain gauges, while the quantities were smaller by the PERSIANN-CCS QPEs. A postprocessing algorithm was adopted in this paper to correct the rainfall results by the 2 weather models. The karst flood simulation and forecasting results showed that the flood peak flow simulations were better by coupling the Karst-Liuxihe model with the PERSIANN-CCS QPEs, and coupling the Karst-Liuxihe model with WRF QPF could extend the lead time of flood forecasting largely, as a maximum lead time of 96 hours can provide an adequate amount of time for flood warnings and emergency responses. The satisfying and rational karst flood simulation evaluation indices proved that coupling the 2 weather models with the new Karst-Liuxihe model could be effectively used for karst river basins, which provides great practical application prospects for karst flood simulations and forecasting. In addition, the postprocessing method used to revise the 2 weather models in this paper is feasible and effective, and this method can largely improve the coupled model application effectiveness and prospect in karst river basins.

1 Introduction

In karst areas, the general lack of long-term meteorological data, especially precipitation data, is a great challenge to the simulation and forecasting of flood events based on

https://doi.org/10.5194/hess-2019-285
Preprint. Discussion started: 8 August 2019

hydrological models (Li et al., 2019). Quantitative Precipitation Forecasts and Estimates (QPF and QPEs) are methods that may enable precipitation data in karst river basins to be easily obtained. The Weather Research and Forecasting (WRF) model, a type of QPF technology, is regarded as a new generation mesoscale weather forecasting model that could provide rainfall data with high accuracy at 1-10 km horizontal resolution (Skamarock et al., 2005). Furthermore, the WRF QPF can forecast rainfall data with a long lead time in karst areas, which is very important for flood warnings and mitigation because more time is provided for flood emergency responses (Tingsanchali, 2012). In this study, the maximum lead time is 96 hours, which can be the greatest factor of concern for decision makers in flood forecasting (Han et al., 2007). The PERSIANN-CCS is a QPE technology by weather satellites, which could estimate long-term and high-resolution rainfall data (Yang et al., 2004, 2007). However, only a few studies of rainfall forecasting based on WRF QPF and PERSIANN-CCS QPEs have been conducted in karst areas until now, and even if there are studies, the practical accuracy is generally poor. In addition, the flood simulation and forecasting results of coupling these weather models with hydrological models have poor precision in karst river basins due to the system error stack of the models as well as the complex hydrogeological conditions of karst water-bearing media (Ford and Williams, 1989; Kovacs and Perrochet, 2011).

Generally, there are only a few rain gauges in karst river basins. Especially in the upstream areas of the basins, which comprise mountains and valleys with complex topographies, it is difficult to set up rain gauges to effectively obtain rainfall data. The study area in this paper is the Liujiang basin with 5.8×10^4 km^2 drainage area; however, there are only 66 rain gauges. On average, there is only approximately 1 rain gauge per 1,000 km^2, and the representativeness is too weak to reflect the actual rainfall that occurs in the basin. Under these circumstances, effective precipitation results could potentially be acquired by using numerical weather models in karst river basins. In recent years, numerical weather prediction models have become increasingly mature with the great progress of the 3S (the remote sensing/RS, geography information system/GIS, and global positioning system/GPS) technologies and can provide a global range of rainfall forecasting products with reasonable and high precision.

The current mainstream numerical weather models include the European Centre Weather Forecasts model (Molteni et al., 1996), the Japan Meteorological Agency weather model (Takenaka et al., 2011), the QPEs by weather radars (Rafieei et al., 2014; Delrieu et al., 2014; Faure et al., 2015), WRF QPF (Skamarock et al., 2008), satellite QPEs (Bartsotas et al., 2017; Wardhana et al., 2017), and others. Among these weather models, WRF QPF and PERSIANN-CCS QPEs may be better ways to acquire precipitation results effectively in karst basins. The lead time of the QPF by the latest WRF model is 1-15 days (Ahlgrimm et al., 2016). Therefore, coupling the hydrological model with WRF QPF for floods warning and

https://doi.org/10.5194/hess-2019-285
Preprint. Discussion started: 8 August 2019

forecasting, the lead time could be extended greatly (Zappa et al., 2010). In comparison to this model, the observed precipitation by rain gauges has no lead time because the precipitation has already fallen to the ground. The lead time of WRF QPF in this study was 96 hours. That is, the equivalent of a 96-hour lead time of flood forecasting, which is very important for the safe transfer of people and property before the floods. PERSIANN-CCS QPEs could offer reasonable rainfall data with high precision, and coupling this model with the distributed hydrological model gave good results in karst flood simulations (Ji et al., 2019).

Several scholars at home and abroad have achieved acceptable results using numerical weather models (Hu et al., 2013; Stenz, 2014; Bartsotas et al., 2017; Wardhana et al., 2017). However, some uncertainty remains that cannot be neglected in the model application, which results in the poor precision of these weather models (Goudenhoofdt and Delobbe, 2009). In this study, 2 effective measures could be used to reduce the uncertainty and improve the precision of the weather models in the karst river basins. One is to choose a suitable model spatial resolution, which could largely affect modelling effects. A initial spatial resolution for WRF QPF and PERSIANN-CCS QPEs are 20 km×20 km and 0.04°×0.04°, respectively. After many tests, the best spatial resolution for the 2 weather models in the study area is 200 m×200 m, which can well match the hydrological model in this paper. The other measure is to reduce the systematic errors of the weather models. A postprocessing algorithm was proposed in this paper to correct WRF QPF and PERSIANN-CCS QPE results in the karst area, which could reduce the rainfall result uncertainties and make the results easier to receive and more credible.

A hydrological model, as a physics-mathematics computational tool, is an important method used to accurately simulate and forecast flood events. Where the precipitation occurs, which is the hydrological model input data, could be the driving factor in flood forecasting (Li et al., 2017). Coupling a hydrological model with WRF QPF and PERSIANN-CCS QPEs has a great capacity and prospect for floods simulations and forecasting in karst areas. However, the traditional hydrological models such as lumped models have considerable disadvantages in karst flood simulations and forecasting. The complex hydrogeological conditions and highly anisotropic karst aquifers as well as water-bearing media in karst areas cause flood processes to be more complex and nonlinear than those in non-karst basins (Goldscheider and Drew, 2007; Hartmann et al., 2013). Lumped hydrological models have a simple model structure, and only a few hydrogeological data are required for modelling. These models usually treat the catchment as a whole unit and ignore the spatial variations in rainfall-runoff as well as the complexity of the underground space structure of karst aquifers (White, 2007). Additionally, the lumped model parameters are homogenized or generalized, and the same set of parameters are adopted for the whole basin, which results in poor precision of flood forecasting applications in karst areas (Scanlon et al., 2003). Physically based distributed hydrological models have great application potential and capabilities in

https://doi.org/10.5194/hess-2019-285
Preprint. Discussion started: 8 August 2019

improving the performance of karst flood event forecasting than lumped hydrological models (Ambroise et al., 1996). In a karst river basin, the entire basin could be divided into many grid units known as the karst sub-basins by the DEM data in the distributed models, and by coupling the grid rainfall with WRF QPF and PERSIANN-CCS QPEs, the actual karst development characteristics and rainfall-runoff processes can be precisely reflected. Therefore, the distributed hydrological models are better than the lumped models for flood simulations and forecasting in karst river basins. To improve the performance and precision, in this study, the karst subbasins will be further divided into smaller grid units known as karst hydrology response units (KHRUs) in the distributed hydrological model.

Shustert and White (1971) made a good attempt to use a distributed model in karst areas. After that, an increasing number of distributed models have been used in karst flood forecasting (Quinlan and Ewers, 1985; Ambroise et al., 1996; White, 2002, 2005, 2007; Gallegos et al., 2013). Ghasemizadeh (2012) introduced several commonly used distributed hydrological models and their application effects in karst watersheds. However, there are 2 obvious shortcomings with the distributed hydrological models when used in karst areas. One is the problem of an insufficient data supply. In particular, it is highly challenging to build distributed models because of the lack of necessary hydrogeological data. The other is the problem of model calculation efficiency. In general, there are many parameters in the distributed models, which require many computational resources, which leads to low efficiency (Chen et al., 2017). In this paper, the hydrogeological data problem is solved by a field survey and tracing test as well as a drill-hole pumping test. In addition, the property data of the study area, including the DEM data, the soil types and the land use types, could be downloaded expediently from the internet at no cost. An improved Particle Swarm Optimization method (Chen et al., 2016) was used for parameter optimization, and the use of this algorithm could improve the computing efficiency of the distributed model and reduce the uncertainty in the parameters.

Currently, there is no unified, widely agreed upon and highly practical distributed karst hydrological model being used around the world. Some distributed models may work accurately in the local area but may not be transferable to another karst basin. Moreover, no such model with high precision could be generally applicable to a typical karst watershed in southwest China, where karst is the most developed. Therefore, we hope to find a distributed hydrological model that has general applicability to the karst area in southwest China through the application of the model proposed in this study. In this paper, the feasibility and application effects of coupling a new karst hydrological model, i.e., the Karst-Liuxihe model with WRF QPF and PERSIANN-CCS QPEs in karst floods simulations and forecasting are studied. Conducting this study served 2 purposes: one purpose was to synthetically compare the performances of WRF QPF and PERSIANN-CCS QPEs in rainfall forecasting in the study area. The other purpose was to verify the performance and feasibility of karst flood

https://doi.org/10.5194/hess-2019-285
Preprint. Discussion started: 8 August 2019

simulations by coupling the 2 weather models with the new Karst-Liuxihe model. The new Karst-Liuxihe model is improved by adding the karst mechanism based on the Liuxihe model prototype (Chen, 2009). The improvements are described below: (1) The karst water-bearing medium is simplified in the model settings. (2) The model structure is refined, as the minimal model structure is divided into KHRUs in this study. (3) The karst mechanism is added to the model calculation, where the calculation principle of the fluid migration rule in the epikarst zone is increased, including the flow movement rule in the shallow karst fissure network; the unsaturated zone, the rapid flow and the slow flow in the model are divided, and the hydraulic relationship between the karst fissure and the conduit systems is calculated. (4) The calculation principle of the groundwater confluence to the basin outlet is improved. (5) Some necessary hydrogeological parameters that are suitable for karst aquifers are added to the model, including the permeability coefficient *K* and so on. There are 14 parameters in the original Liuxihe model, and the parameter number increased to 20 in the Karst-Liuxihe model.

In this study, both weather models, i.e., WRF QPF and PERSIANN-CCS QPEs, can provide high-resolution grid rainfall data, which are coupled with the Karst-Liuxihe model could make a satisfactory effect in karst floods simulations and forecasting. This model is applied to the Liujiang karst basin, which is the area of China where karst is the most developed. The karst flood simulation effect of the coupled model is excellent. In particular, the simulation error of the flood peak flow is effectively controlled. Moreover, the maximum lead time of rainfall forecasting can reach 96 hours, which makes a significant difference for flood warnings and the secure transfer of people and property before the occurrence of flooding. The coupling proposed in this study could be applied to other karst river basins in China and even around the world due to the reasonable and acceptable flood simulation effects.

2 Study area and data

2.1 Geology and landforms

The study area of this paper is the Liujiang karst river basin, which located at 23.9°~24.5°N, 108.9°~109.7°E in southwest China. The channel length of Liujiang river is about 1,120 km and the area is about 5.8×10^4 km^2. It is the most developed karst basin of China, as shown in Fig. 1a, the map of Liujiang watershed. The carbonate rocks distribution area is about 1.9×10^4 km^2, which are mainly distributed in the northern part of the watershed. The peak forest plain in the downstream basin and the peak cluster depression in the middle and upper reaches are the dominant landforms of the study area. The karst valley is the main landform in the south, where the underlying bedrock, which mainly comprises carbonate and dolomite. A large area of limestone is distributed in the western part, where the peak cluster depression is dominant. Hilly and mountain are the dominant landforms in the eastern part. In particular, the highest mountain in the basin is Leigong Mountain, which has an elevation of 2124 m (as shown in Fig. 1b) and is located in the northeast basin. The dominant landforms in the central part and downstream are the peak forest plains.

Figure 1. The sketch map of Liujiang karst watershed.

The upstream area of the basin is located in the southern part of the ancient Paleocaledonian fold belt and the southeastern edge of the southwest China depositional area, where a large area of sedimentary rock is distributed. The outcrop strata in the basin are ancient and intact and mainly include Sinian, Cambrian, Silurian, Ordovician, Upper Devonian, Lower Carboniferous, Upper Permian, Lower Triassic, Paleogene, Quaternary Pleistocene and Holocene.

After a long karst landform evolutionary process, karst development in the basin is now very mature. At first, there were mainly small karst doline funnels in the basin; then, the landform evolved into a peak cluster depression (as shown in Fig. 2, photographs of the middle and upper reaches) as carbonate rocks continued to be eroded by karst water as well as the fluviraption of allogeneic water, especially the Liujiang River. Under these interior erosional effects and exterior fluviraption for so many years, the geomorphological evolution reached an old age, i.e., the peak cluster depressions had evolved to the peak forests (Williams, 1987), especially in the downstream (as shown in Fig. 2, photograph of the downstream reaches).

Figure 2. The karst landform evolution of the Liujiang basin.

2.2 Precipitation, karst flood and property data

The Liujiang River, a rain-source river, the average annual precipitation in the basin is between 1400 and 1700 mm. The flood season is from May to September, and the flood volume can account for 80% of total runoff. The maximum peak flow is 2.59×10^4 m^3 s^{-1} (in 2009, as shown in Fig.12 in the section 6.3). The water level rise over a 24-hour period can be as high as 12.1 m (in 1978). The mean annual maximum flood peak discharge is 15,200 m^3 s^{-1}, and the maximum 7-day mean flood volume is 5.38 billion m^3. In the upper reaches, most of the landforms are deep-cut canyons shaped like a “V” except in the river source regions. The elevation of these canyons is usually greater than 1000 m with a relative height of 500~700 m (as shown in Fig. 1b). In these canyons, the runoff responds quickly to rainfall, and the area is prone to regional flood disasters.

The flood characteristics are closely related to rainstorms, the watershed topography and the karst landform. Larger floods are mostly multipeak processes, and an increase lasts only a short period of time, i.e., the flood peak occurs quickly and recedes quickly in terms of the flood response, which usually causes considerable damage. In the 1990s, the frequency and

https://doi.org/10.5194/hess-2019-285
Preprint. Discussion started: 8 August 2019

Hydrology and Earth System Sciences
Discussions

intensity of rainstorms and flood disasters were increasing with the increase in extreme weather. The north-eastern and western areas of the basin are the main flood sources, and this the area where the most developed karst is located. Especially the karst conduits are well developed in the underground aquifer. According to the tracing test conducted in Liujiang basin, during the flood season, the flood velocity can reach to 43-130 km/d. The maximal velocity is 173 km/d, which indicates the karst underground rivers are well developed in the study area. The karst features can significantly affect the hydrologic process, especially during the rainfall-runoff process in the model. It is highly challenging to accurately simulate the karst water cycle rules and forecast the floods changeable trends in the future.

In the study area, there are total of 66 rain gauges, 156 grid gauges for WRF QPF and 131 grid gauges for PERSIANN-CCS QPEs (as shown in Fig. 1a), respectively. And 5 floods that occurred from 2008-2013 were used to verify the performance of coupling the Karst-Liuxihe model with WRF QPF and PERSIANN-CCS QPEs. Hourly precipitation from the rain gauges was adopted to revise the products of the 2 weather models in this paper. The property data of the watershed are mainly the DEM data, the soil types as well as the land use types. These property data could be downloaded easily from the internet at no cost: (1) The DEM data are from http://srtm.csi.cgiar.org, last accessed: 02 April 2019. (2) The land use types can be downloaded from http://landcover.usgs.gov, last accessed: 02 April 2019. (3) The soil types are from http://www.isric.org, last accessed: 05 April 2019. After resampling in the ArcGIS 10.2, these property data are downscaled to the same resolution as the hydrological model in this paper.

3 WRF QPF and PERSIANN-CCS QPEs

3.1 WRF QPF12

The WRF QPF used in this study was the WRF Advanced Research model version 3.4 (Skamarock et al., 2008), which is a 3-dimensional and nonhydrostatic system that can forecast complex weather changes on cloud scale and synoptic scale well. This model is especially precise at 1-10 km horizontal resolution, which can satisfy the practical application requirements of rainfall forecasting in this study. WRF QPF was applied in this study using the following configurations: (1) The domain of the WRF QPF model is set at 24 °N and 109 °E, as the location of the basin is 23.9 °~24.5 °N, 108.9 °~109.7 °E. (2) The vertical structure of the model includes 28 levels with the Lambert conformal projection (Li et al., 2015). (3) The initial temporal and spatial resolutions were 3-hour and 20 km × 20 km, respectively. Following downscaling, the temporal and spatial resolutions were 1-hour and 200 m × 200 m, respectively. The downscaled method, which was calculated in ArcGIS 10.2 through the statistical scales relationship between the DEM data and weather model (Fan et al., 2017). (4) The entire basin was covered by 156 grid gauges based on the WRF QPF. The rainfall forecasting was produced with a lead time of 96 hours (other results of lead times such as 24, 48 and 72 h have also been calculated (Li et al., 2017)). (5) The WRF QPF results were evaluated and revised by comparing the rainfall data from the rain gauges.

The WRF QPF parameters were set according to the following configurations: (1) The single-moment, 3-class microphysics parameterization is used in this study (Hong and Lim, 2006). (2) The Yonsei University (YSU) planetary boundary layer scheme and the Kain-Fritsch cumulus parameterization (Kain, 2004) are adopted to optimize the cumulus parameters. (3) Other physics schemes for the model parameters used in this paper include the Goddard scheme (Chou and Suarez, 1994), Rapid Radiative Transfer Model (Mlawer et al., 1997) and the NOAH scheme (Ek et al., 2003). More details on the WRF QPF model and its parameter settings can be found in the research results of previous studies (Li et al., 2015; Li et al., 2017).

3.2 PERSIANN-CCS QPEs

The PERSIANN-CCS QPEs (Yang et al., 2004, 2007), which is developed based on the PERSIANN prototype system (Hsu et al., 1999); this system is a next-generation rainfall estimation system based on geostationary satellites that use computer imaging technology and pattern recognition technology. The PERSIANN-CCS QPE system was based on geostationary infrared imagery and daytime visible imagery (Soroosh et al., 2000). The system is automated for estimating precipitation through the use of satellite remote sensing technology. The parameters of the PERSIANN system could be optimized efficiently by a self-adaptive artificial neural network (Yang et al., 2007).

The model setup, parameter optimization and rainfall estimation procedures of PERSIANN-CCS (Hsu, 2007; Li et al., 2017) can be found in operating manuals and user guides from http://chrs.web.uci.edu/projects_nasa.php, last accessed: 15 April 2019. However, in practical application, the PERSIANN-CCS QPE model does not have to be built to obtain the rainfall data in a particular study area. Worldwide products of QPEs based on the PERSIANN-CCS including the rainfall results in this paper could be easily downloaded at no cost from http://cics.umd.edu/ipwg/us_web.html, last accessed: 18 March 2019. Therefore, the rainfall data from the PERSIANN-CCS QPEs could be obtained expediently in karst areas where rain gauges are usually lacking.

The specific operational steps for the PERSIANN-CCS QPEs in this study area are as follows: (1) Determine the time and scope of the study area, i.e., the rainfall occurrence and end time as well as the location according to the longitude and latitude. (2) Download the estimated precipitation data by the PERSIANN-CCS. (3) Analyze and appraise the products of PERSIANN-CCS QPEs by comparing the observed rainfall by rain gauges. (4) Revise the PERSIANN-CCS QPEs products by using appropriate methods.

The PERSIANN-CCS QPE products can generate precipitation data at a time interval of

30 min and a spatial resolution of 0.04 °×0.04 °(Yang et al., 2007). The spatial resolution was downscaled to 200 m×200 m using a downscaling method (Fan et al., 2017) to suit the resolution of the Karst-Liuxihe model in this paper. The time interval was changed to 1 hour.

3.3 Forecasting and evaluation of the precipitation results

There are total of 66 rain gauges, 156 grid gauges of WRF QPF and 131 grid gauges of PERSIANN-CCS QPEs in this study area, respectively. These grid gauges can cover the entire basin (as shown in Fig. 1a) and provide a representative rainfall product. The WRF QPF model offers rainfall forecasting with a lead time of 96 hours, while the rainfall estimation results of PERSIANN-CCS have no lead time. The hourly precipitation data for 2008, 2009, 2011, 2012 and 2013 from the products of the 2 weather models were produced, compared and revised in this study by using the observed precipitation data of rain gauge. The forecasting, estimation and comparison of the rainfall results by the 3 precipitation products, i.e., the WRF QPF model, the PERSIANN-CCS QPEs, and the rain gauge precipitation are shown in Figs. 3, 4, 5, 6 and 7, respectively.

Figure 3. The rainfall results of the 3 precipitation products (2008).

Figure 4. The rainfall results of the 3 precipitation products (2009).

Figure 5. The rainfall results of the 3 precipitation products (2011).

Figure 6. The rainfall results of the 3 precipitation products (2012).

Figure 7. The rainfall results of the 3 precipitation products (2013).

Figs. 3-7 showed the average value of the rainfall results of the WRF QPF model, the PERSIANN-CCS QPEs, and the rain gauge precipitation, where (a), (b), and (c) are the average values of the rainfall results according to the rain gauge, WRF QPF, and PERSIANN-CCS QPEs, respectively. (d) and (e) are the quantile-quantile plot, a 45-degree line here is drawn to compare the rainfall results of the 2 weather models and the rain gauge precipitation, respectively.

According to the results shown in Figs. 3-7, the rainfall distributions appeared to be quite similar with WRF QPF, the PERSIANN-CCS QPEs, and observed precipitation by rain gauge. Especially from Figs.3-7 (d) and (e), the 2 precipitation plots, i.e., WRF QPF and the rain gauge precipitation, PERSIANN-CCS QPEs and the precipitation by rain gauge were very closely distributed around the 45-degree lines, meant the distribution of these 3 rainfall products were close to one another. However, a relative error of the 3 rainfall products cannot be ignored. The results from the WRF QPF were larger than those from the rain gauges, while the PERSIANN-CCS QPEs were smaller, which meant that relative errors exist between the weather model precipitation values and the rain gauge precipitation.

To further quantitatively evaluate and compare the rainfall results of the 2 weather models with the rain gauge precipitation, the average precipitations of the 3 rainfall products were listed in Table 1.

Table 1. The quantitative rainfall comparison results of the 3 precipitation products.

From the rainfall results listed in Table 1, some relative errors between the 2 weather models and the rain gauge precipitation cannot be ignored. The average precipitation values of WRF QPF were larger than the rain gauge precipitation, while the PERSIANN-CCS QPEs values were smaller. The relative errors between the PERSIANN-CCS QPEs and the precipitation by rain gauge were less than those of the WRF QPF and the rain gauge precipitation. The rainfall estimation results according to PERSIANN-CCS had no lead time, while the WRF QPF model offered rainfall forecasting with a lead time of 96 hours, which meant a lead time of 96 hours for flood forecasting by coupling the Karst-Liuxihe model with WRF QPF model in this study.

The average relative errors were 17% and -14% for WRF QPF and PERSIANN-CCS QPEs, respectively. These errors are considerable relative errors and cannot be ignored. Therefore, an effective method should be used to reduce these relative errors and make the rainfall results by the 2 weather models more credible and receivable.

3.4 Postprocessing of the 2 weather models

To make the quantitative values of the rainfall results from WRF QPF and PERSIANN-CCS QPEs closer to those of the observed precipitation by rain gauge, which means to make the forecasting rainfall results are more credible, the precipitation products according to the 2 weather models were revised using the rain gauge precipitation that was considered as the true precipitation of the basin. The procedures of postprocessing the 2 precipitation products are as follows.

1. The average values of WRF QPF and PERSIANN-CCS QPEs were calculated according to this equation:

$$\bar{P}_{\text{WRF/PERSIANN-CCS}} = \frac{\sum_{i=1}^{N} P_i F_i}{N} \tag{1}$$

where $\bar{P}_{\text{WRF/PERSIANN-CCS}}$ are the average values of the precipitation results based on WRF QPF and PERSIANN-CCS QPEs, P_i is the precipitation of the 2 weather models at i grid gauge, F_i are the watershed areas of i grid gauge, and N are the grid gauges numbers.

2. Average values of the observed precipitation based on rain gauge by this equation:

https://doi.org/10.5194/hess-2019-285
Preprint. Discussion started: 8 August 2019

$$\bar{P}_2 = \frac{\sum_{j=1}^{M} P_j}{M} \qquad (2)$$

where $\bar{P}_2$ are the average values of the rain gauge precipitation, M are the rain gauge numbers, and P_j are the average values of the observed precipitation of j rain gauge.

3. Average values of the rain gauge precipitations were adopted to correct the WRF QPF and PERSIANN-CCS QPEs using this equation:

$$P_i^{'} = P_i \frac{\bar{P}_2}{\bar{P}_{\text{WRF/PERSIANN-CCS}}} \qquad (3)$$

where $P_i^{'}$ is the quantitative value of the precipitation according to WRF QPF and PERSIANN-CCS QPEs after revision at i grid gauge, and P_i are the precipitation values of the 2 weather models at the *i* grid gauge.

This postprocessing method made the rainfall results based on the PERSIANN-CCS QPEs and WRF QPF closer to the observed rainfall results by rain gauges, which can largely reduce the systematic errors of the 2 weather models. Therefore, the revision method described in this study was feasible. After the postprocessing, the precipitation products based on the 2 weather models were fed into the Karst-Liuxihe model to validate the model's feasibility in karst flood events simulations and forecasting in the study area.

4 Hydrological model

4.1 The Liuxihe model

The Liuxihe model, a fully physically-based distributed hydrological model, was proposed by Y, Chen (Chen, 2009), and this model earned its name through the first significant successes in flood forecasting in the Liuxihe River basin, Guangdong Province, China. The Liuxihe model has achieved many reasonable and gratifying research results in the past decade (Chen, 2009, 2018; Fan et al., 2012; Liao et al., 2012; Chen et al., 2016, 2017), which is especially significant for flood forecasting in some reservoirs and catchments (Li et al., 2017, 2019; Hui et al., 2018).

The entire structure of Liuxihe model is divided into 7 sub-models, including the watershed delineator and data mining sub-model, the unit classification and section estimation sub-model, the rainfall fusion calculation sub-model, the evapotranspiration

https://doi.org/10.5194/hess-2019-285
Preprint. Discussion started: 8 August 2019

Hydrology and Earth System Sciences Discussions
Open Access
EGU

calculation sub-model, the rainfall-runoff calculation sub-model, the confluence calculation sub-model, the parameter sensitivity analysis and the parameter optimization sub-model. In the vertical structure of the Liuxihe model, there are 3 layers from top to bottom: the canopy layers, the soil layers and the underground layers, respectively. And the horizontal structure is also divided into 3 types: the river cells, the hill slope cells and the reservoir cells. More details of the Liuxihe model structure and its application effects can be found in the studies by Chen (2009, 2018) and Li (2017, 2019).

4.2 Karst-Liuxihe model

The Liuxihe model prototype is a terrestrial hydrological mechanism model, which is particularly useful in rainfall-runoff and confluence calculations, as the model performs well in forecasting the river surface. To be suitable for karst basins, the structure of the Liuxihe model should be improved to effectively adapt to the complex karst hydrogeological conditions, which involves adding the karst mechanism to the model. A new distributed hydrological model in this study, the Karst-Liuxihe model, was proposed on the prototype of Liuxihe model to simulate and forecast the karst flood events. The process of improving the structure of the Karst-Liuxihe model is summarized as follows.

1. Make the karst water-bearing media simplification in the model

In general, the karst hydrological process is hard to accurately forecast using a hydrological model due to the complicated and anisotropic hydrogeological conditions of the karst aquifers. Therefore, the water-bearing media in the karst aquifer must be effectively simplified before building the model. First, the karst underground river system was generalized into a multiple spatial structure in the model, where the water movement rules of the underground river could be intelligible and computable. Second, the groundwater movement patterns are divided into slow flow and rapid flow in the model. Slow flow mainly exists in the tiny karst fissures, and rapid flow mainly occurs in wide karst cracks, conduits, sinkholes and the underground river. Atkinson (1977) noted that when the width of the karst fissure exceeds 10 cm, the water flow in the karst water-bearing medium is a non-Darcy flow, i.e., turbulence with a rapid speed. The 10-cm width of the karst fissure was treated as a threshold in this study, and when the width exceeded 10 cm, the groundwater movement pattern was divided by the rapid flow. Otherwise, the flow was slow flow. In fact, a threshold of 10 cm is sufficient in terms of contribution to flooding, especially for such a large study area (5.8×10^4 km^2).

2. Refine model structure and divide into KHRUs

The entire study area would be divided into a lot of grid cells by the high-resolution DEM data, and these grid cells are known as karst sub-basins. The confluence path for each karst sub-basin to the outlet of the basin is clear. Furthermore, to be suitable for the complex karst aquifer and water-bearing media in karst basins, the model structure must be fine enough to meet the flood simulation and forecasting requirements. Therefore, the karst subbasins can be further divided into many KHRUs using GIS technology combined with the karst landform in this paper, and the spatial variations in the karst subbasins can be subtly described. Each KHRU had its own model parameters, and calculations of the entire karst hydrological process, including calculations of precipitation, evapotranspiration, rainfall-runoff and confluence, are independent of each other in each KHRU. This type of multiple spatial structure in the model could effectively make maximum use of the limited meteorological and hydrogeological data. In the vertical structure of the KHRU in the Karst-Liuxihe model, there are 5 layers, including the vegetation cover, the soil layer, the epikarst zone, the bedrock layer as well as the underground river. Water movement and exchange rules between the karst fissure and conduit in the epikarst zone were reasonably considered in this study. Fig. 8 shows the structure map of the KHRU.

a. The structure of the KHRU and the partial enlarged detail

b. A picture of the KHRU

Figure 8. The 3-dimensional spatial structure of the KHRU.

In Fig. 8, the partially enlarged details of Fig. 8a and b show the 3-dimensional spatial model of the KHRU that is built in our laboratory, which is used to observe the slow and rapid flows transfer into the karst fissures and conduits more intuitively. This process may be necessary and helpful for modelling.

3. Increase the calculation of water movement rules in the karst aquifers

There is no module to address the water movement rules in the epikarst zone in the Liuxihe model prototype. In the Karst-Liuxihe model in this study, the karst aquifer system was divided into karst fissure and conduit systems, in which the water movement rule was divided into slow flow and rapid flow. The 10-cm width of the karst crack is a threshold (Atkinson, 1977); when the width exceeds 10 cm, the water movement pattern is divided by the rapid flow. Otherwise, the flow is the slow flow. The karst fissure systems were mainly the rock matrix and some small fissures, while the conduit systems include the wide fissures and conduits as well as the karst shaft, sinkhole, and underground river during the floods. The water movement was slow in the small karst fissure system and obeys Darcy's law. Therefore, in the Karst-Liuxihe model, the system was generalized to an equivalent porous medium. A 3-dimensional equation of groundwater motion was used to describe the slow flow:

$$\frac{\partial}{\partial x}\left(K_{xx}\frac{\partial h}{\partial x}\right)+\frac{\partial}{\partial y}\left(K_{yy}\frac{\partial h}{\partial y}\right)+\frac{\partial}{\partial z}\left(K_{zz}\frac{\partial h}{\partial z}\right)\pm W=S_s\left(\frac{\partial h}{\partial t}\right) \tag{4}$$

where K_{xx}, K_{yy}, and K_{zz} are the permeability coefficients of the rock mass in the *X*, *Y*, and

https://doi.org/10.5194/hess-2019-285
Preprint. Discussion started: 8 August 2019

Hydrology and Earth System Sciences
Open Access
Discussions

Z directions, respectively, m d^{-1}; *h* is the groundwater head, m; *W* is the source-sink term, d^{-1}; S_s is the storage coefficient, m^{-1}; and *t* is the time, d.

The conduit systems were generalized to multiple circular tubes, considering that the tubes were mostly under pressure during the floods. Thus, the conduit systems were bearing tubes in this paper. In these bearing tubes, when the groundwater was in a state of laminar flow, the water flows of the tubes were calculated by the Hagen-Poiseuille equation:

$$Q = -A\frac{gd^2\partial h}{32\nu\partial x} = -A\frac{\rho g d^2 \Delta h}{32\mu\tau\Delta l} \tag{5}$$

where *Q* is the water flow of the laminar flow, m^3 s^{-1}; *A* is the tube cross-sectional area, m^2; *d* is the pipe diameter, m; ρ is the density of the underground water, kg m^{-3}; g is gravity acceleration, m s^{-2}; $\nu = \mu / \rho$ is the coefficient of kinematic viscosity, and this value can be calculated from the temperature (Shoemaker, 2008); $\partial h / \partial x = \Delta h / \tau\Delta l$ is the hydraulic slope of the tubes, and τ is the tube curvature, which is a dimensionless parameter here.

When the groundwater was in a state of turbulent flow, the water flows of the tubes were calculated by the Darcy-Weisbach equation:

$$\begin{aligned} Q &= -2A\log\left(\frac{k_c}{3.71d} + \frac{2.51\nu}{d\sqrt{\dfrac{2gd\partial h_c}{\partial x}}}\right)\sqrt{\frac{2gd\partial h_c}{\partial x}} \\ &= -2A\sqrt{\frac{2gd\,|\Delta h|}{\Delta l\tau}}\log\left(\frac{k_c}{3.71d} + \frac{2.51\nu}{d\sqrt{\dfrac{2gd^3|\Delta h|}{\Delta l\tau}}}\right)\frac{\Delta h}{|\Delta h|} \end{aligned} \tag{6}$$

where *Q* is the water flow of the turbulent flow, m^3 s^{-1}; f is the friction factor, dimensionless here; k_c is the average tube wall height, m; $R_e = Vd / \nu$ is the Reynolds Number, and V is the average velocity of the tubes, m s^{-1}. The Reynolds Number is divided into the upper Reynolds Number and the lower Reynolds Number to determine whether the flow in the tubes is laminar and turbulent. When there was laminar flow, the Reynolds Number at that time was greater than the upper Reynolds Number. Then, the groundwater in the tubes transitioned from laminar flow to turbulent flow. When there was turbulent flow, the Reynolds Number at that time was less than the lower Reynolds Number, and the groundwater in the tubes transitioned from turbulent flow to laminar flow.

In the unsaturated zone of the karst aquifer, there is usually an exchange of water between slow flow and rapid flow, i.e., the exchange of water exists between each conduit

Hydrology and Earth System Sciences
Discussions

node and the connecting fissure node, and the exchange of water flow could be calculated using this equation:

$$\begin{cases} Q=\alpha_{i,j,k}\left(h_n-h_{i,j,k}\right) \\ \alpha_{i,j,k}=\sum_{ip=1}^{np}\dfrac{\left(K_w\right)_{i,j,k}\pi d_{ip}\dfrac{1}{2}\left(\Delta l_{ip}\tau_{ip}\right)}{r_{ip}} \end{cases} \tag{7}$$

where $\alpha_{i,j,k}$ is the exchange coefficient at grid cell i, j, k of the KHRU, m^2 s^{-1}; h_n is the head value of the corresponding tube node, m; $h_{i,j,k}$ is the head value of the grid cell i, j, k, m; *np* is the tube number than connected the i, j, k tube node; $\left(K_w\right)_{i,j,k}$ is the permeability coefficient of the tube wall, m d^{-1}; d_{ip} is the pipe diameter of tube *ip*, m; Δl_{ip} is the length of the connection between the i and p tube node, m; τ_{ip} is the tube curvature, and r_{ip} is the tube radius, m.

4. Add some necessary hydrogeological parameters to the model

In the original Liuxihe model, there are 14 parameters that require optimization, and after adding the karst mechanism and especially by adding some necessary hydrogeological parameters in the Karst-Liuxihe model. Then, the parameters were increased to 20, and among them 18 need to be optimized. The remaining 2 parameters were the flow direction and slope, which can be directly calculated from the high-resolution DEM data.

These added parameters could represent the underground water movement rules in the epikarst zone and the underground river. The 6 added parameters are the macro crack volume ratio, *V*; the permeability coefficient, *K*; the specific yield of the aquifer, *χ*; thickness of the karst aquifer, *h*; depletion coefficient, *ω;* and channel roughness, n_1. The parameters added into the Karst-Liuxihe model will inevitably lead to uncertainties in the model during flood simulation and forecasting, so the parameter sensitivity must be effectively analysed and evaluated. In this study, a parameter sensitivity analysis method, known as the multiparameter sensitivity analysis (MPSA) by Choi (1999) et al., was developed based on the Generalised likelihood uncertainty estimation (GLUE) method to evaluate the parameter sensitivity in the model.

5. Coupled model set up

5.1 Model setup

In general, there are many pits in the karst areas, and some of which are the false pits.

https://doi.org/10.5194/hess-2019-285
Preprint. Discussion started: 8 August 2019

Hydrology and Earth System Sciences
Discussions

The existence of false pits is due to wrong data and systematic errors of DEM itself. These false pits need to be reasonably filled before building the coupled model. Because there are karst depressions and sinkholes in the karst areas, which cause true pits to exist, the model retained these true pits, including the depressions and sinkholes. These true pits in the study area play an important role in the flood transmission process and can be found through a field survey. Due to the detention effect and peak clipping in the karst depressions, the hydrological process is delayed, especially for the flood peak flow. This effect must be considered in the coupled model, which can make a better performance for the model in karst flood events simulations and forecasting. Before building the model, whether there exists a detention effect and peak clipping in the karst depressions and sinkholes in the study area is a key factor. If so, the storage capacity and size of these pits must be determined by a field survey during floods. The capacity can be deduced according to the water level, and the amounts of stranded floods near the pits must be considered in the water balance calculation in the model. The specific calculation steps in the coupled model are shown below.

1. First, the limit discharge capacity of the underground river entrance in the study area, i.e., Q_{max}, was deduced through a field investigation and monitoring.
2. Then, the water inflow from the entrance of the underground river, i.e., Q_{in}, can be calculated through the coupled model.
3. The relationship between Q_{in} and Q_{max} was compared to determine whether the flood detention phenomenon was generated.

If $Q_{in} > Q_{max}$, the flood detention phenomenon is generated, and then, the flow of the underground river outlet, $Q_{out=} Q_{max}$ is generated. The water storage of the flood detention from the entrance of the underground river, Q_s, is as follows:

$$Q_s = Q_{s1}+Q_{in}-Q_{max} \tag{8}$$

where Q_s is the water storage of the flood detention during this period, $m^3\ s^{-1}$; Q_{s1} is the water storage of the flood detention from the preceding time period, $m^3\ s^{-1}$; and if there is no flood detention, i.e., Q_{s1}=0.

If $Q_{in} \leq Q_{max}$, and Q_{s1}=0, then

$$Q_{out=} Q_{in} \tag{9}$$

If $Q_{in} \leq Q_{max}$, Q_{s1}>0, and $Q_{in}+ Q_{s1} \leq Q_{max}$, then

$$Q_{out=} Q_{in}+ Q_{s1} \tag{10}$$

Otherwise, if $Q_{in} \leq Q_{max}$, Q_{s1}>0, and $Q_{in}+ Q_{s1}> Q_{max}$, then

$$Q_{out=} Q_{max} \tag{11}$$

https://doi.org/10.5194/hess-2019-285
Preprint. Discussion started: 8 August 2019

In this study, the entire karst basin was divided into 1,469,900 KHRUs in the Karst-Liuxihe model using the 200 m×200 m high-resolution DEM data. There were 6,696 river cells and 1,463,204 hill slope cells. The river system was divided into a 4-order stream based on Strahler's method, which is shown in Fig. 1a. The KHRU in the coupled model (Fig. 8), which is the smallest unit, was proposed to effectively reflect the complicated hydrogeological condition of the underlying surface and karst aquifers. All the hydrological processes, including evapotranspiration and rainfall-runoff, confluence as well as the parameter optimization, were calculated on this KHRU and because the KHRU was completely physically-based, the differences in the complex hydrogeological characteristics of karst aquifers could be truly reflected. Therefore, the model effect and performance in karst forecasting could be reliably improved in this way.

After division of the KHRUs, i.e., model setup was finished, the postprocessed WRF QPF and the PERSIANN-CCS QPEs results were fed into the Karst-Liuxihe model to validate its feasibility in karst floods simulations and forecasting.

5.2 Parameter optimization

There are 20 parameters in the Karst-Liuxihe model, and among these parameters, 18 needed to be optimized. In this study, an improved PSO algorithm, mainly the algorithm parameters, were revised to improve the performance and convergence efficiency (Chen et al., 2016); this improvement can largely improve the accuracy of the coupled model in flood simulations and forecasting in a karst basin. The observed rainfall and karst flood event data as well as the hydrogeological data of the karst underlying the surface and aquifer were adopted to optimize the parameters of the Karst-Liuxihe model in this paper. These data were fully physically-based that can describe the complex karst water-bearing medium effectively.

There are 30 floods in the study area from 1982-2013, which were used to verify the model effect in the karst hydrological processes simulations and prediction. The flood prediction results were very good (Li et al., 2019), implied that the model can be effectively applied in karst areas. In this study, 8 karst flood events, including floods 2005061400, 2006060400, 2007070800, 2008060900, 200906090800, 201106010900, 201206022000 and 201306011400, were used to test the coupled model performance in the karst floods forecasting, i.e., coupling the Karst-Liuxihe model with the 2 weather models, WRF QPF and PERSIANN-CCS QPEs. Among these flood events, floods 2005061400, 2006060400, 2007070800 and 2008060900 were used for parameter optimization, and the best flood simulation based on these four floods was used for the final parameter optimization. The remainder of the floods were adopted for model validation. The parameter evolution results of the coupled model are shown in Fig. 9.

Figure 9. The parameter evolution results.

https://doi.org/10.5194/hess-2019-285
Preprint. Discussion started: 8 August 2019

6 Results and discussion

6.1 Results of the parameter optimization

From the parameter evolution results in Fig. 9, the parameter evolution process began very volatile, and after a few cycles, approximately 20 times, the evolution leveled off and held steady after 40 cycles, which signified that the parameter optimization had converged. The thickness of a lines in Fig. 9 indicates the sensitivity of the parameters, and the thicker the line is, the more sensitive the parameter will be. The sensitivity of the parameters will be elaborated upon in the next section of the paper (section 6.2). The karst floods simulation effects based on parameter optimization were drawn in Fig. 10, and the evaluation indices of the flood simulations were listed in Table 2.

Figure 10. The karst floods simulation effects of the coupled model.

Table 2. Evaluation indices for the karst floods simulation effects.

From Fig. 10, the karst flood simulated effect of flood 2008060900 was the best, especially for the simulated flood peak flow, was the closest to observed peak flow. To further compare the effects of the flood simulations, the 6 evaluation indices, including the Nash-Sutcliffe coefficient/C; the coefficient of the water balance/W; the correlation coefficient/R; the flood peak flow relative error/E%; the process relative error/P% as well as the flood peak flow time error/T(hours), were listed in Table 2. These indices were also the best for modelling flood 2008060900. Therefore, flood 2008060900 was finally used for the parameter optimization. The reasonable simulated flood processes based on the improved PSO algorithm for the coupled model were suited the practically observed values very well (as shown in Fig. 10 and Table 2), which implied that the parametric optimization method in this study, i.e., the improved PSO algorithm was feasible and effective.

6.2 Model uncertainty analysis

The uncertainty analysis of the coupled model in this study could be effectively solved with 3 aspects: 1. Ensure the reliability of the model input data, which include rainfall data, karst flood events, and hydrogeological data. Among these data, the rainfall data can be reliably obtained by WRF QPF and PERSIANN-CCS QPEs; the karst flood events were obtained from the local hydrology department, and the hydrogeological data were obtained through a field survey and tracer testing in the study area. 2. Solve the uncertainty problem of model structure through model structure and function improvement (as shown in section 4.2). 3. Solve the uncertainty problem of the model parameters.

The uncertainty analysis of the parameters for the coupled model mainly means the parameters sensitivity analysis in this study. The sensitivity analysis method used in this paper, which is known as MPSA (Choi et al., 1999), was improved on the Generalized Likelihood Uncertainty Estimation (GLUE) algorithm. The Nash-Sutcliffe coefficient/C, as the objective function, was used to analyse the sensitivity of the coupled model parameters in this study, the equation of the objective function was as follows:

$$NSE = 1 - \frac{\sum_{i=1}^{n}\left(Q_i - Q_i^{'}\right)^2}{\sum_{i=1}^{n}\left(Q_i - \overline{Q}\right)^2} \tag{12}$$

where NSE was the value of the objective function, i.e., Nash-Sutcliffe coefficient/C; Q_i and $Q_i^{'}$ were observed and simulated water flows, respectively, $m^3 s^{-1}$, $\overline{Q}$ was the average observed water flow value, $m^3 s^{-1}$, and n was the observed period numbers, hours.

Table 3 shows the results of the parameters sensitivity calculation. In Table 3, the closer the value of the objective function for the parameter is to 1, the more sensitive the parameter will be.

Table 3. The calculation results of the coupled model parameters sensitivity.

From the results shown in Table 3, the value of the objective function for the parameter-saturated water content, θ_{sat} was the maximum one. This means that the parameter, θ_{sat} is the most sensitive parameter of the Karst-Liuxihe model. The parameter sensitivity is also shown in Fig. 9. The thickness of the line in Fig. 9 indicates the parameter sensitivity, and the thicker the line, the more sensitive the parameter will be, which can represent the sensitivity of parameters more intuitively. From Table 4 and Fig. 9, the sequence of parameter sensitivity of the Karst-Liuxihe model was as follows: $\theta_{sat} > \theta_s > \theta_{fc} > K_s > V > K > \chi > h > z > b > S_w > S_p > n > n_1 > \omega > \lambda > E_p > C_{wl}$. The name of these parameters are shown in Table 3.

6.3 Floods simulations with the postprocessed 2 weather models

In this study, to analyse the effects of the karst flood simulation using the initial WRF QPF, the PERSIANN-CCS QPEs and their postprocessed results, the karst flood events, floods from 2008-2013 were simulated by the coupled model. The results comparisons are shown in Fig. 11 to Fig. 15.

Figure 11. The flood simulation results of flood 2008060900 based on the coupled model. (a) is the postprocessed WRF flood simulation result, and (b) is the postprocessed PERSIANN-CCS flood simulation result.

Figure 12. The flood simulation results of flood 200906090800 based on the coupled model. (a) is the postprocessed WRF flood simulation result, and (b) is the postprocessed PERSIANN-CCS flood simulation result.

Figure 13. The flood simulation results of flood 201106010900 based on the coupled model. (a) is the postprocessed WRF flood simulation result, and (b) is the postprocessed PERSIANN-CCS flood simulation result.

https://doi.org/10.5194/hess-2019-285
Preprint. Discussion started: 8 August 2019

Figure 14. The flood simulation results of flood 201206022000 based on the coupled model. (a) is the postprocessed WRF flood simulation result, and (b) is the postprocessed PERSIANN-CCS flood simulation result.

Figure 15. The flood simulation results of flood 201306011400 based on the coupled model. (a) is the postprocessed WRF flood simulation result, and (b) is the postprocessed PERSIANN-CCS flood simulation result.

From Fig. 11 to Fig. 15, the floods simulations with the original WRF QPF and PERSIANN-CCS QPEs products were unsatisfactory, especially for the simulated peak flows. In contrast, the coupled model performance with the postprocessed WRF QPF and PERSIANN-CCS QPEs were better. The simulated flood peak errors of the postprocessed weather models were effectively reduced. For further comparison, the 6 evaluation indices of the floods simulations with the original weather models and the postprocessed models are shown in Table 4.

Table 4. The evaluation indices of karst floods simulations with the original WRF QPF and PERSIANN-CCS QPEs and their postprocessed values.

From Table 4, all of these 6 evaluation indices with the postprocessed WRF QPF and PERSIANN-CCS QPEs had improved than those with the original 2 weather models. For the WRF QPF, after postprocessing, the average water balance coefficient increased by 8%;the average Nash-Sutcliffe coefficient increased by 3%; and the average correlation coefficient increased by 2%. While the average process relative error decreased by 5%; the average peak flow relative error decreased by 5%;and the peak flow time error decreased by 2 hours, respectively. For the postprocessing PERSIANN-CCS QPEs, the average Nash-Sutcliffe coefficient increased by 5%; the average water balance coefficient increased by 4%; and the average correlation coefficient increased by 4%; While the average process relative error decreased by 5%; the average peak flow relative error decreased by 6%; and the average peak flow time error decreased by 3 hours, respectively. Obviously these evaluation indices were getting better following postprocessing of WRF QPF and PERSIANN-CCS QPEs, which implied that the postprocessing method for the 2 weather models in this study was effective and reasonable.

6.4 Verify the coupled model performance by comparing 3 kinds of precipitation products

There are 3 kinds of precipitation products that are used in this study, i.e., rain gauge precipitation, postprocessed WRF QPF and postprocessed PERSIANN-CCS QPEs. The effects of different types of precipitation products on the flood process simulated by hydrological model are calculated and compared to test their performance. The flood events included floods from 2008-2013, which were simulated by the coupled model. The results comparison is shown in Fig. 16, and Table 5.

https://doi.org/10.5194/hess-2019-285
Preprint. Discussion started: 8 August 2019

Figure 16. The karst floods simulated effects of the coupled model with the 3 precipitation products.

Table 5. The evaluation indices of karst floods simulations with the 3 precipitation products.

From Fig. 16 and Table 5, the flood processes simulated by the Karst-Liuxihe model using the rain gauge precipitation were better than those of the postprocessed WRF QPF and PERSIANN-CCS QPEs. The rain gauge precipitation can directly reflect the actual rainfall situation in the basin, which is the reason that the rain gauge precipitation, taken as the true value, was used to calibrate the weather models in this paper. However, this kind of precipitation based on rain gauge measurements has no lead time because the rain has fallen to the ground. In addition, there is usually a shortage of rain gauges in karst areas. Therefore, the WRF QPF and the PERSIANN-CCS QPEs were adopted to obtain the effective precipitation in the study area. From Fig. 16 and Table 5, compared with the karst flood processes simulated with the postprocessed WRF QPF, the flood simulated results with the postprocessed PERSIANN-CCS QPEs were slightly better. In particular, the peak flow simulation demonstrated the superiority of the postprocessed PERSIANN-CCS QPEs. However, the rainfall estimation results from PERSIANN-CCS have no lead time, while the WRF QPF can offer rainfall forecasting with a lead time of 96 hours, which means that there is a lead time of 96 hours for flood forecasting by coupling the Karst-Liuxihe model with the WRF QPF. This lead time of the coupled model can provide more responses time for floods warnings.

The satisfying flood simulated results in Fig. 16 and their rational evaluation indices in Table 5 proved that coupling the 2 weather models with the Karst-Liuxihe model in this paper was feasible and effective for the Liujiang basin. In particular, the flood detention and peak clipping effect of the upstream karst depressions were considered in the coupled model calculation, making the water balance calculation in the model more reasonable and reflecting the actual flood evolution process in the karst area; the average coefficients of water balance/ W for the precipitation by rain gauges, WRF QPF and PERSIANN-CCS QPEs were 0.92, 1.07, and 0.89, respectively (as shown in Table 5). The water amount is basically balanced in the model. Furthermore, the flood detention effect made the flood peak appear later in reality, and by contrast, the simulated peak flow time came earlier, despite the flood detention effect being considered in the model. The average peak time error, T for the rain gauge precipitation, WRF QPF and PERSIANN-CCS QPEs were -5, -6, and -4, respectively. In some ways, these results provide an extra amount of lead time for flood forecasting. The peak clipping effect considered in the coupled model brought the simulated peak flow value closer to that of the observed value. The average peak flow relative error, E for the rain gauge precipitation, WRF QPF and PERSIANN-CCS QPEs were 4%, 12%, and 8%, respectively (as shown in Table 5).

Therefore, coupling the Karst-Liuxihe model with the postprocessed WRF QPF and PERSIANN-CCS QPEs could largely improve the precision of the karst flood simulations and forecasting.

7 Conclusion

The precipitation result, as a hydrological model input data, is one of the driving factors that makes the model work swimmingly. However, it is often hard to acquire effective rainfall results in karst areas. In this paper, WRF QPF and PERSIANN-CCS QPEs were adopted to obtain acceptable precipitation results for the Liujiang karst river basin. A postprocessed method was proposed to revise the rainfall products using these 2 weather models. To test the effectiveness of this revision, the Karst-Liuxihe model was coupled with the postprocessed WRF QPF and PERSIANN-CCS QPEs to simulate the floods of Liujiang karst watershed. The Karst-Liuxihe model proposed in this study performed well in the flood simulations and forecasting. The model structure and function was improved from various aspects, including refining the model structure by putting forward the KHRUs in the model, increasing the calculations of water movement rules in the epikarst zone and underground river, and by adding some necessary hydrogeological parameters to the coupled model to reflect the true conditions of rainfall-runoff in the karst underlying surface. The reasonable flood events simulated effects by the improved Karst-Liuxihe model proved that the postprocessed method proposed to revise the weather models in this paper was feasible. The following conclusions were obtained from the study results of this paper.

1. The quantitative precipitation results produced by WRF QPF and PERSIANN-CCS QPEs were quite closed to the observed rainfall data by rain gauge, especially in the rainfall distribution. However, there is a relative error between the precipitation of the weather models and the rain gauge, which was 17% with WRF QPF and -14% with PERSIANN-CCS QPEs. This finding implied that WRF QPF overestimated the precipitation value, while PERSIANN-CCS QPEs underestimated the precipitation values. The postprocessing method proposed in this study could largely reduce these relative errors.

2. The model parametric uncertainty analysis showed that the parameter-saturated water content, θ_{sat} was the most sensitive. The parameter sensitivity sequence of the Karst-Liuxihe model was: $\theta_{sat} > \theta_s > \theta_{fc} > K_s > V > K > \chi > h > z > b > S_w > S_p > n > n_1 > \omega > \lambda > E_p > C_{wl}$.

3. Compared with the karst floods events simulated effects based on the initial 2 weather models, the floods simulations with the postprocessed WRF QPF and PERSIANN-CCS QPEs were much better. For the postprocessed WRF QPF, the average water balance coefficient, Nash-Sutcliffe coefficient, and correlation coefficient were increased by 8%,3%,2%, respectively. While the average peak flow relative error, process relative error, and the peak flow time error were decreased by 5%,5%,2 hours, respectively. For the postprocessed

PERSIANN-CCS QPEs, the average water balance coefficient, Nash-Sutcliffe coefficient, and correlation coefficient were increased by 4%,5%,4%, respectively. While the average peak flow relative error, process relative error, and the peak flow time error were decreased by 6%,5%,3 hours, respectively. It was obvious that the postprocessed method proposed in this study was effective and feasible.

4. The flood processes simulated by the Karst-Liuxihe model using the rain gauge precipitation were the best. Compared with the simulated floods with the postprocessed WRF QPF, the simulation effects with the postprocessed PERSIANN-CCS QPEs were slightly better, especially in the peak flow simulation. However, the rainfall data by the PERSIANN-CCS QPEs had no lead time, which was applicable to the simulation and inversion after the occurrence of floods. However, coupling the Karst-Liuxihe model with the WRF QPF model resulted in a lead time of 96 hours in the flood forecasting, which can provide an adequate amount of time for flood warnings and emergency responses. The satisfying flood simulated results proved that coupling the 2 weather models with the Karst-Liuxihe model in this paper was feasible and reasonable for the Liujiang karst river basin.

5. The flood detention and peak clipping effect of the upstream karst depressions were calculated in the coupled model, which enabled the model to reflect the actual flood evolution processes in the study area. The simulated average coefficients of water balance/W for the observed precipitation by rain gauge, WRF QPF and PERSIANN-CCS QPEs were 0.92, 1.07, and 0.89, respectively. The simulated average peak time error, T for the rain gauge precipitation, WRF QPF and PERSIANN-CCS QPEs were -5, -6, and -4, respectively, and in a way, provided extra lead time for the flood warning and forecasting. The simulated average value of the peak flow relative error, E for the rain gauge precipitation, WRF QPF and PERSIANN-CCS QPEs were 4%, 12%, and 8%, respectively, which were close to that of the observation values. These results proved that coupling the Karst-Liuxihe model with the postprocessed WRF QPF and PERSIANN-CCS QPEs in this paper could largely improve the precision of karst floods simulations and forecasting. This coupled model could be effectively adopted in other karst areas like Liujiang karst basin.

Data availability.

The observed rainfall data and the karst flood events are offered by Liuzhou hydrological bureau, Guangxi province, China.

The WRF model for this study is the WRF-ARW model version 3.4; and the PERSIANN-CCS QPEs data can be downloaded at no cost from http://cics.umd.edu/ipwg/us_web.html, last accessed: 18 March 2019. The Liuxihe model prototype is offered by Y, Chen (Chen, 2009).

The property data of the study area, including the DEM data, the land use type and the soil type, can be downloaded at no cost. The DEM data are from http://srtm.csi.cgiar.org, last accessed: 02 April

https://doi.org/10.5194/hess-2019-285
Preprint. Discussion started: 8 August 2019

Hydrology and Earth System Sciences
Open Access
Discussions

2019. Land use types can be downloaded from http://landcover.usgs.gov, last accessed: 02 April 2019. The soil types are from http://www.isric.org, last accessed: 05 April 2019.

Author contributions. The first and corresponding author is JIL, was in charge of the entire paper, such as the model calculation and the writing of this paper and so on. DY provided advice on the scientific issues raised in this article. YJ helped to conceive the structure of the model. JL provided significant assistance in the English translation of the paper. YC offered the prototype of the Liuxihe model.

Competing interests.

The authors declare that they have no conflicts of interest.

Acknowledgments. This study is supported by the National Key Research and Development Program of China (2016YFC0502306), China Postdoctoral Science Foundation (2019M653316), the Fundamental Research Funds for the Central Universities (XDJK2019C017), the Chongqing Municipal Science and Technology Commission Fellowship Fund (No. cstc2018jcyj-yszx0013), the Open Project Program of the Chongqing Key Laboratory of Karst Environment (Grant No. Cqk201801), and the Open Project Program of the Laboratory of Chongqing groundwater resourse utilization and environmental protection.

https://doi.org/10.5194/hess-2019-285
Preprint. Discussion started: 8 August 2019

Hydrology and Earth System Sciences
Open Access
Discussions

Figures

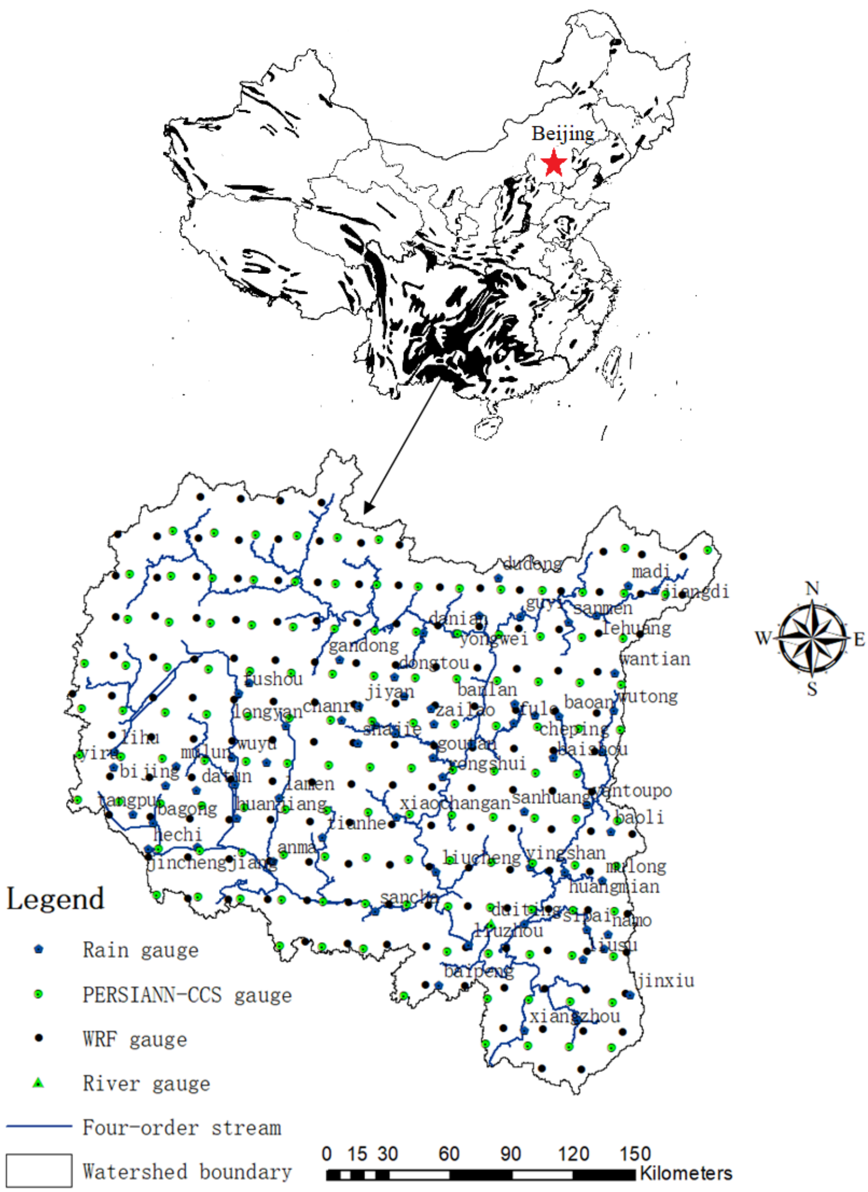

a. Gauges map (The black patches of the map are karst areas)

https://doi.org/10.5194/hess-2019-285
Preprint. Discussion started: 8 August 2019

Hydrology and Earth System Sciences
Discussions

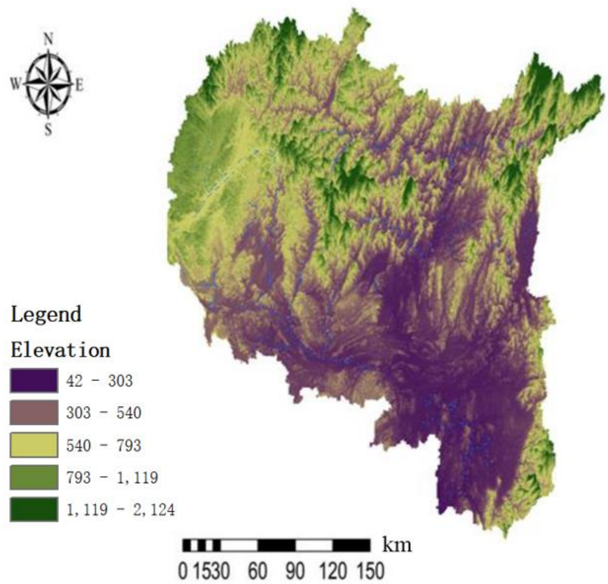

b. Elevation map

Figure 1. The sketch map of Liujiang karst watershed.

https://doi.org/10.5194/hess-2019-285
Preprint. Discussion started: 8 August 2019

Hydrology and Earth System Sciences
Open Access
Discussions

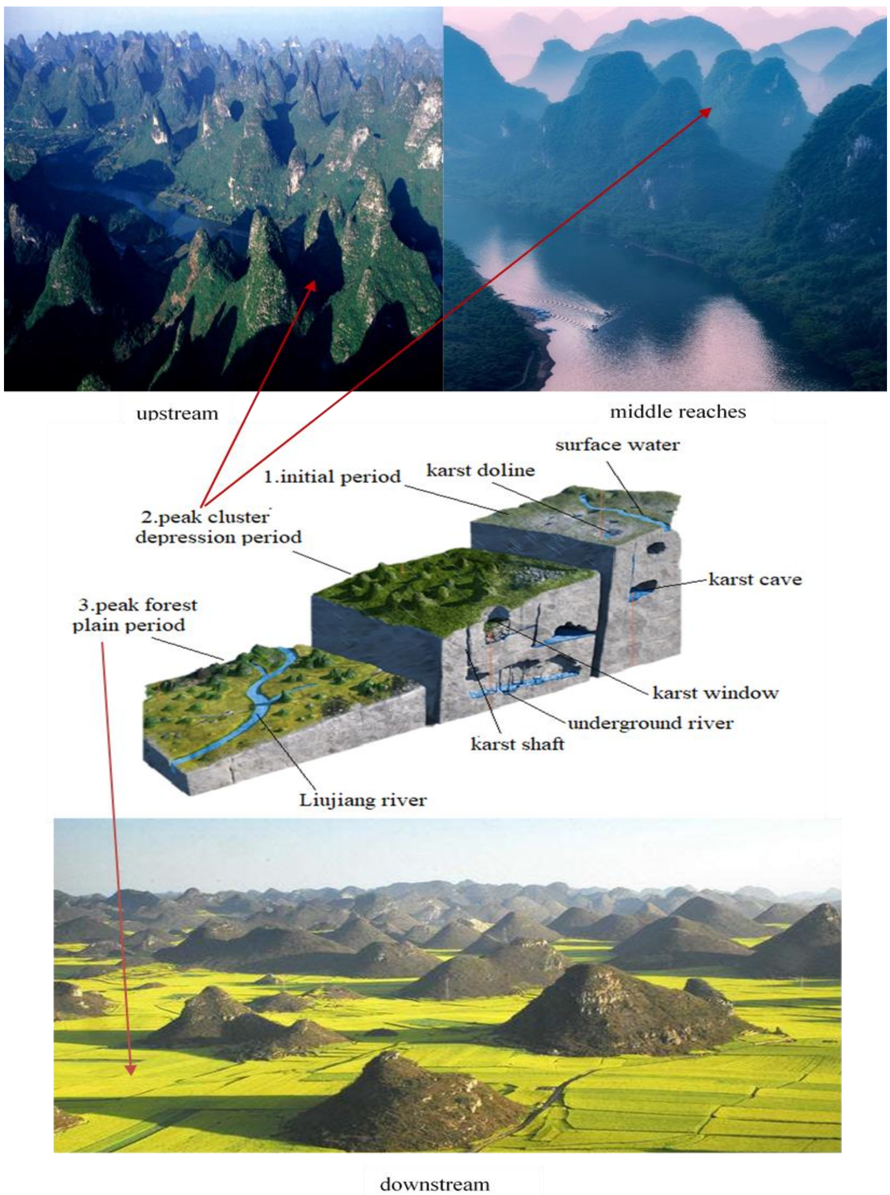

Figure 2. The karst landform evolution of the Liujiang basin（The photographs of the basin upstream is from http://guilinkarst.com/en/nd.jsp?id=113, last access:10 April 2019. The photographs of the middle reaches is captured by planet institute at https://mp.weixin.qq.com/s?mpshare=1&scene=22&mid=2247521167&sn=a3bf8521fda8e297ed58eae7e07bdc67&idx=1&__biz=MzIyOTQ1OTYzMw%3D%3D&chksm=e8408051df3709477da49ef4362bf2f40db5279360c32f118575b71d596af78d098beea814d8&srcid=0402YfBsf64zXrtsVpHoAuHg#rd, last access:2 April 2019. And the photographs of the basin downstream is from http://travel.sohu.com/20130221/n366552284_2.shtml, last access:10 April 2019).

https://doi.org/10.5194/hess-2019-285
Preprint. Discussion started: 8 August 2019

Hydrology and Earth System Sciences
Discussions

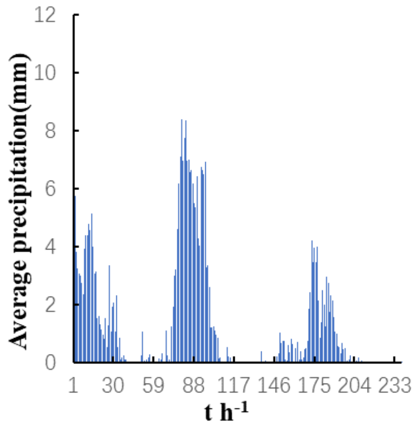

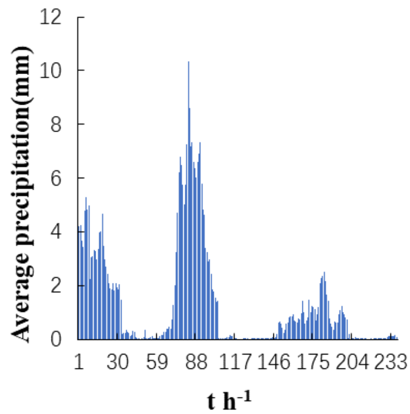

a. Rain gauge precipitation

b. WRF QPF

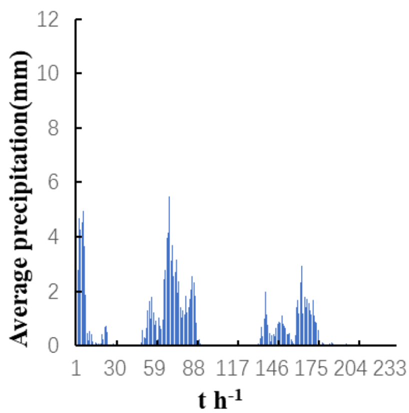

c. PERSIANN-CCS QPEs

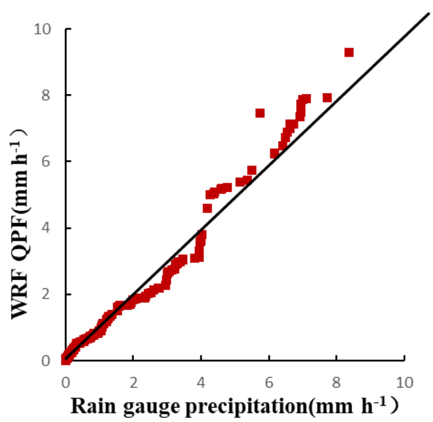

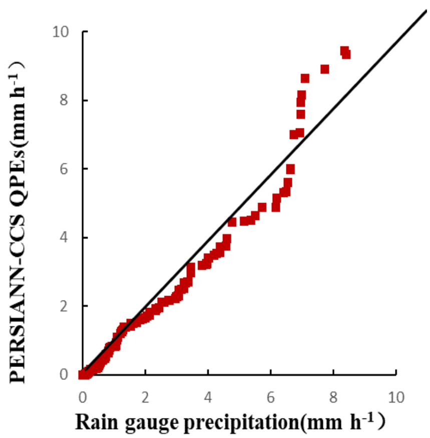

https://doi.org/10.5194/hess-2019-285
Preprint. Discussion started: 8 August 2019

d. Quantile–quantile plot of WRF QPF and Rain gauge precipitation

e. Quantile–quantile plot of PERSIANN-CCS QPEs and Rain gauge precipitation

Figure 3. The rainfall results of the 3 precipitation products (2008).

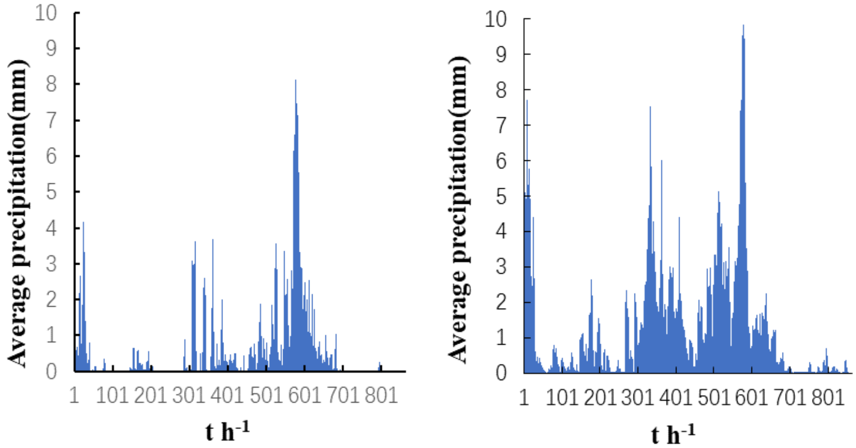

a. Rain gauge precipitation

b. WRF QPF

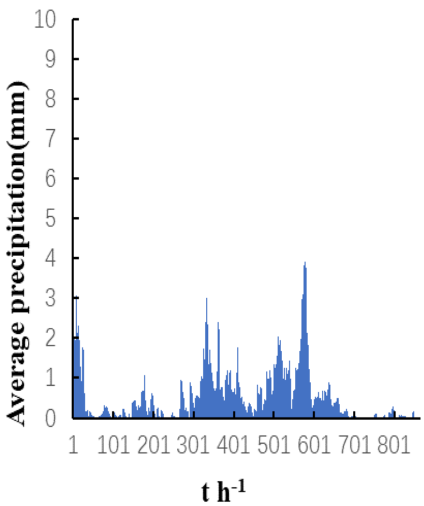

c. PERSIANN-CCS QPEs

https://doi.org/10.5194/hess-2019-285
Preprint. Discussion started: 8 August 2019

Hydrology and Earth System Sciences
Discussions
Open Access

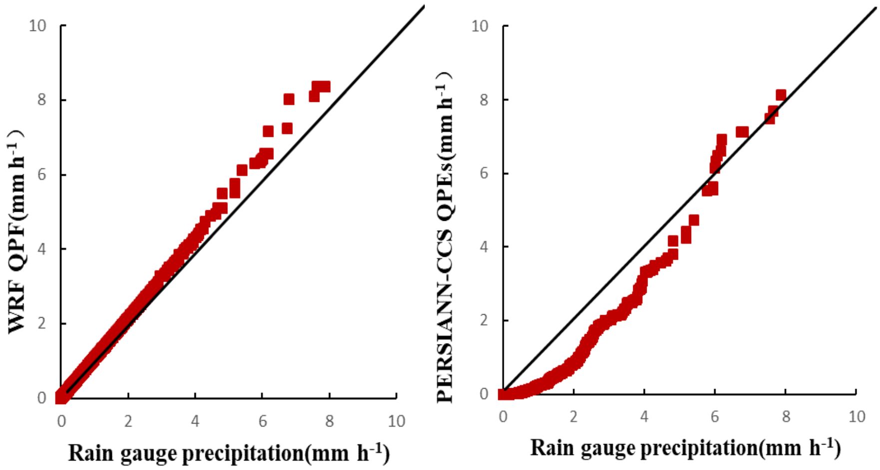

d. Quantile–quantile plot of WRF QPF and Rain gauge precipitation

e. Quantile–quantile plot of PERSIANN-CCS QPEs and Rain gauge precipitation

Figure 4. The rainfall results of the 3 precipitation products (2009).

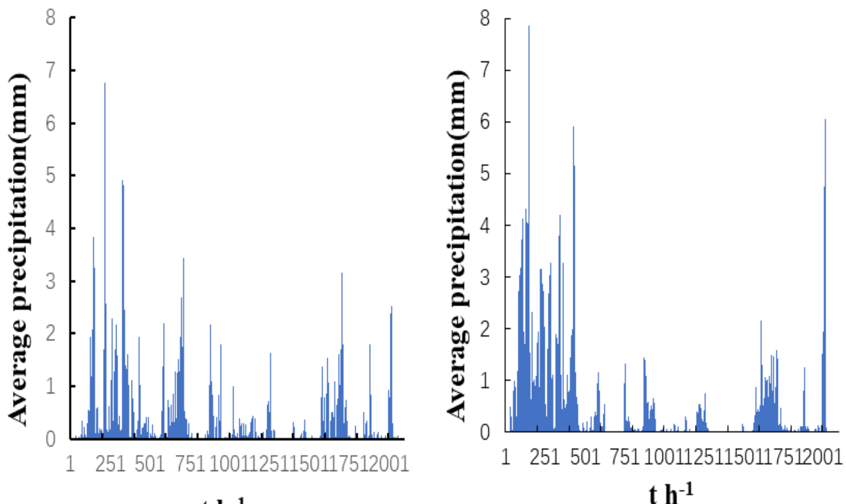

a. Rain gauge precipitation

b. WRF QPF

https://doi.org/10.5194/hess-2019-285
Preprint. Discussion started: 8 August 2019

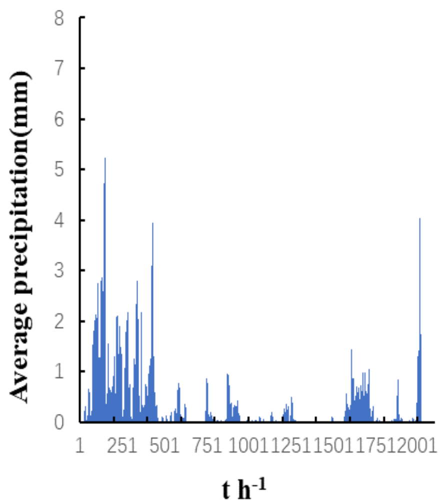

c. PERSIANN-CCS QPEs

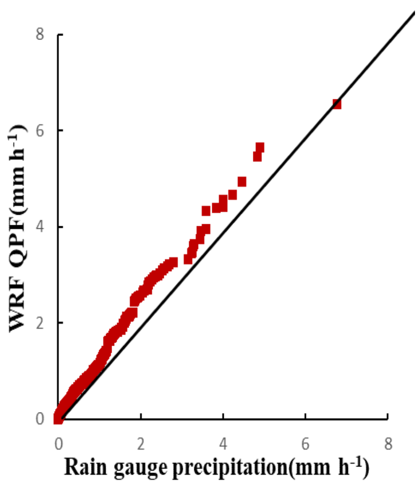

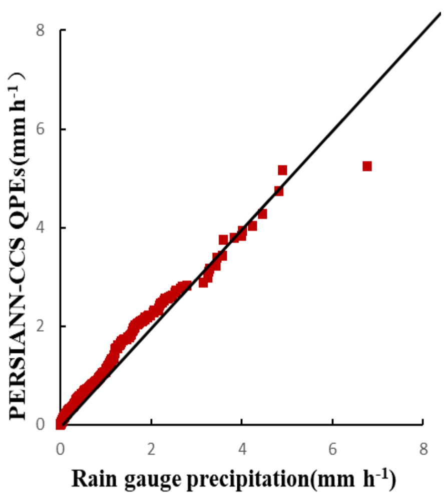

d. Quantile–quantile plot of WRF QPF and Rain gauge precipitation

e. Quantile–quantile plot of PERSIANN-CCS QPEs and Rain gauge precipitation

Figure 5. The rainfall results of the 3 precipitation products (2011).

https://doi.org/10.5194/hess-2019-285
Preprint. Discussion started: 8 August 2019

Hydrology and Earth System Sciences
Discussions

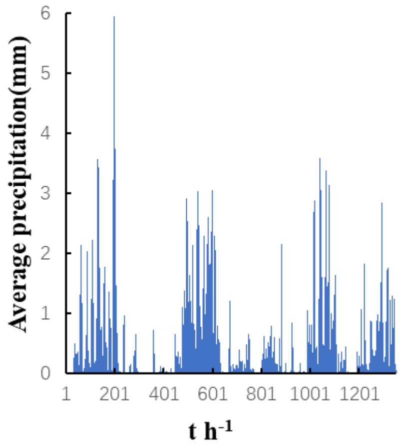

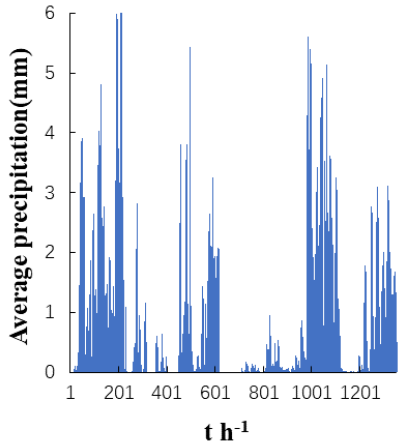

a. Rain gauge precipitation

b. WRF QPF

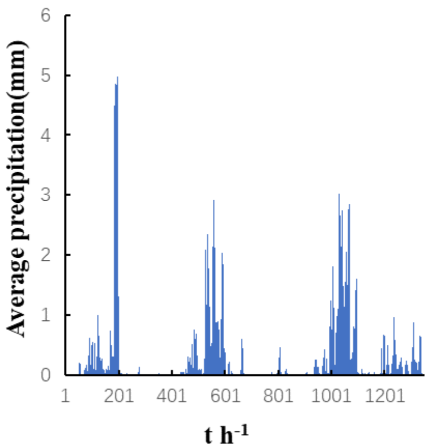

c. PERSIANN-CCS QPEs

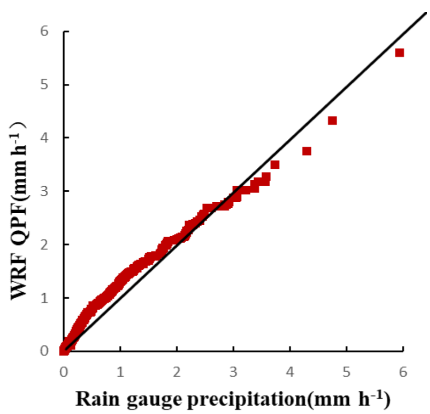

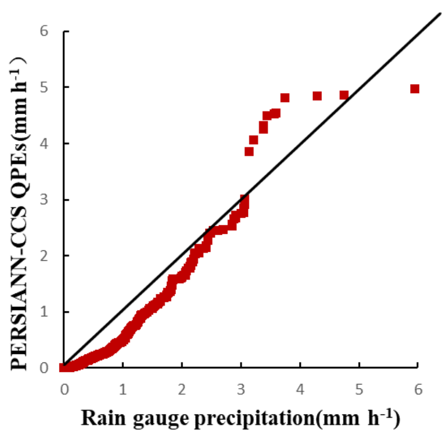

https://doi.org/10.5194/hess-2019-285
Preprint. Discussion started: 8 August 2019

Hydrology and Earth System Sciences
Open Access
Discussions

d. Quantile–quantile plot of WRF QPF and Rain gauge precipitation

e. Quantile–quantile plot of PERSIANN-CCS QPEs and Rain gauge precipitation

Figure 6. The rainfall results of the 3 precipitation products (2012).

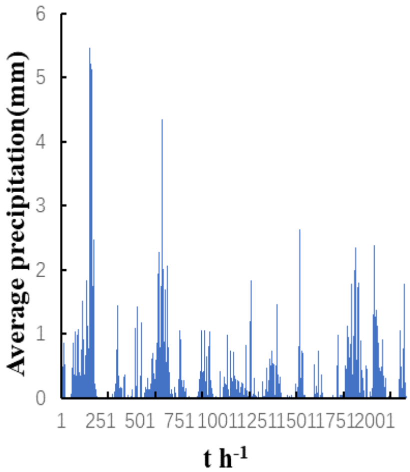

a. Rain gauge precipitation

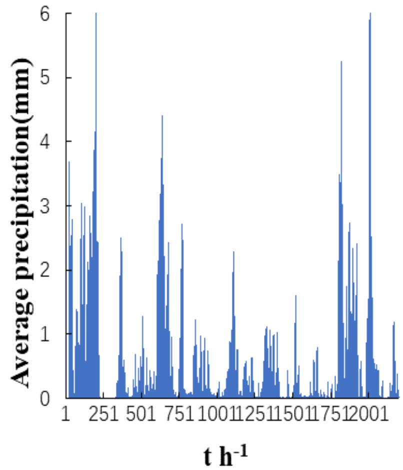

b. WRF

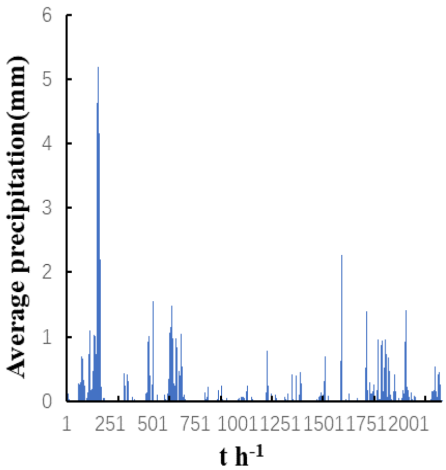

c. PERSIANN-CCS QPEs

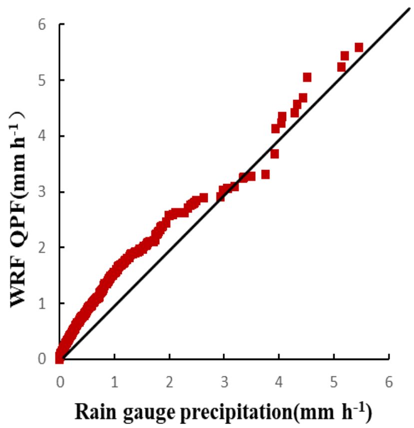

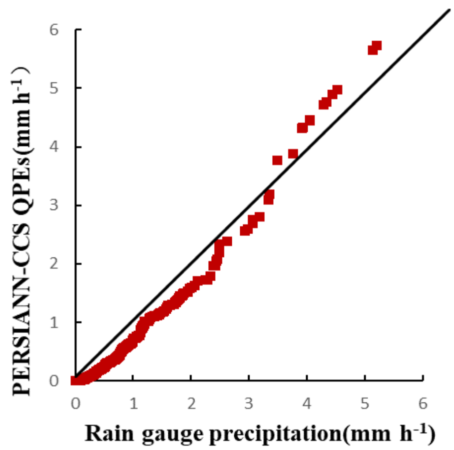

d. Quantile–quantile plot of WRF QPF and Rain gauge precipitation

e. Quantile–quantile plot of PERSIANN-CCS QPEs and Rain gauge precipitation

Figure 7. The rainfall results of the 3 precipitation products (2013).

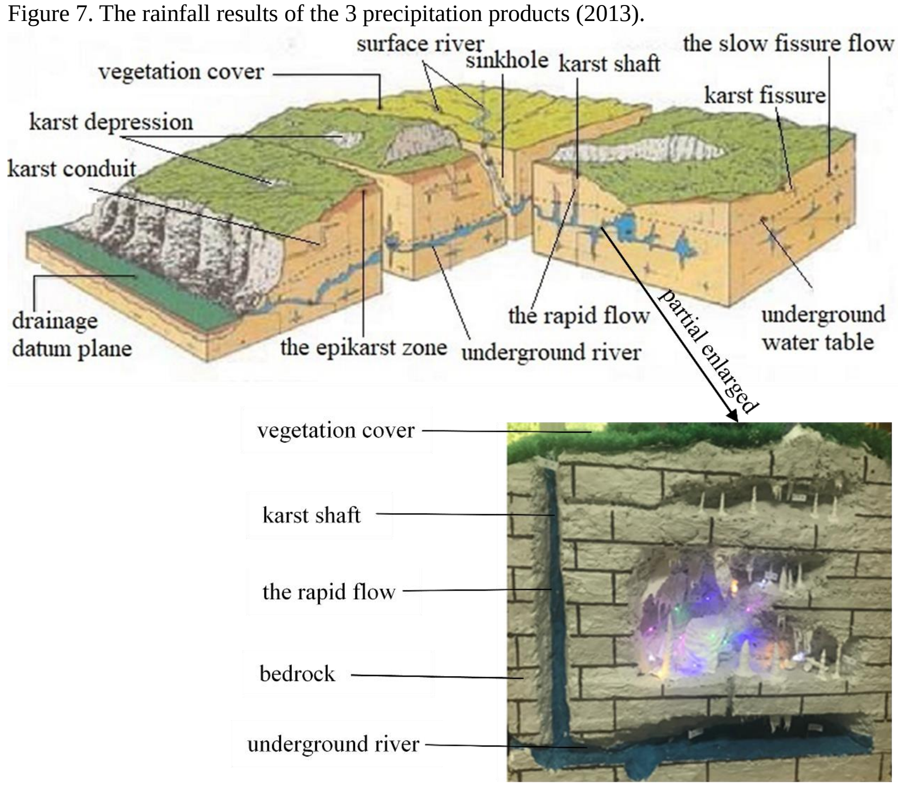

a. The structure of the KHRU and the partial enlarged detail

https://doi.org/10.5194/hess-2019-285
Preprint. Discussion started: 8 August 2019

Hydrology and Earth System Sciences
Discussions

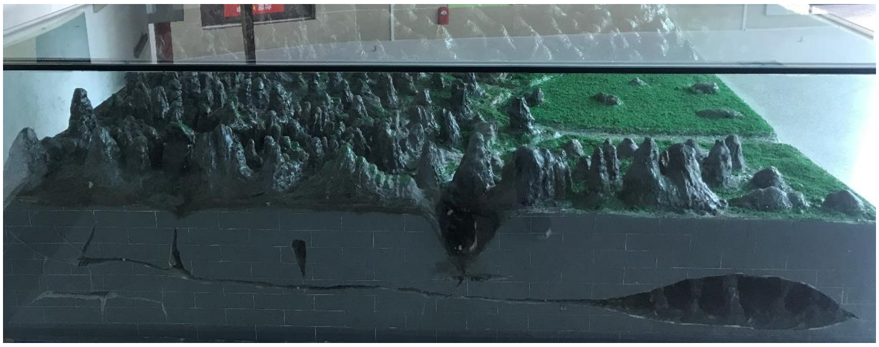

b. A picture of the KHRU

Figure 8. The 3-dimensional spatial structure of the KHRU.

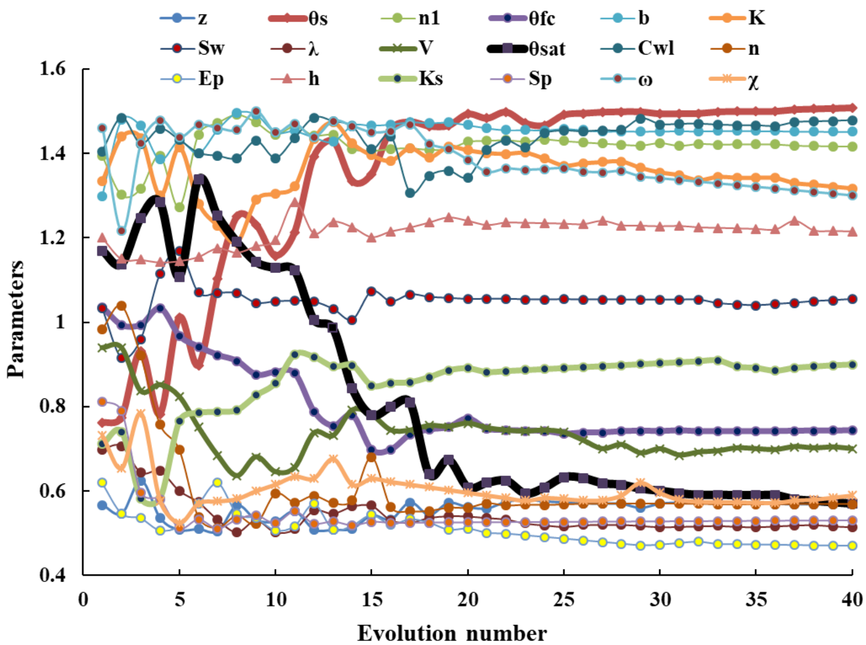

Figure 9. The parameter evolution results.

https://doi.org/10.5194/hess-2019-285
Preprint. Discussion started: 8 August 2019

Hydrology and Earth System Sciences
Open Access
Discussions

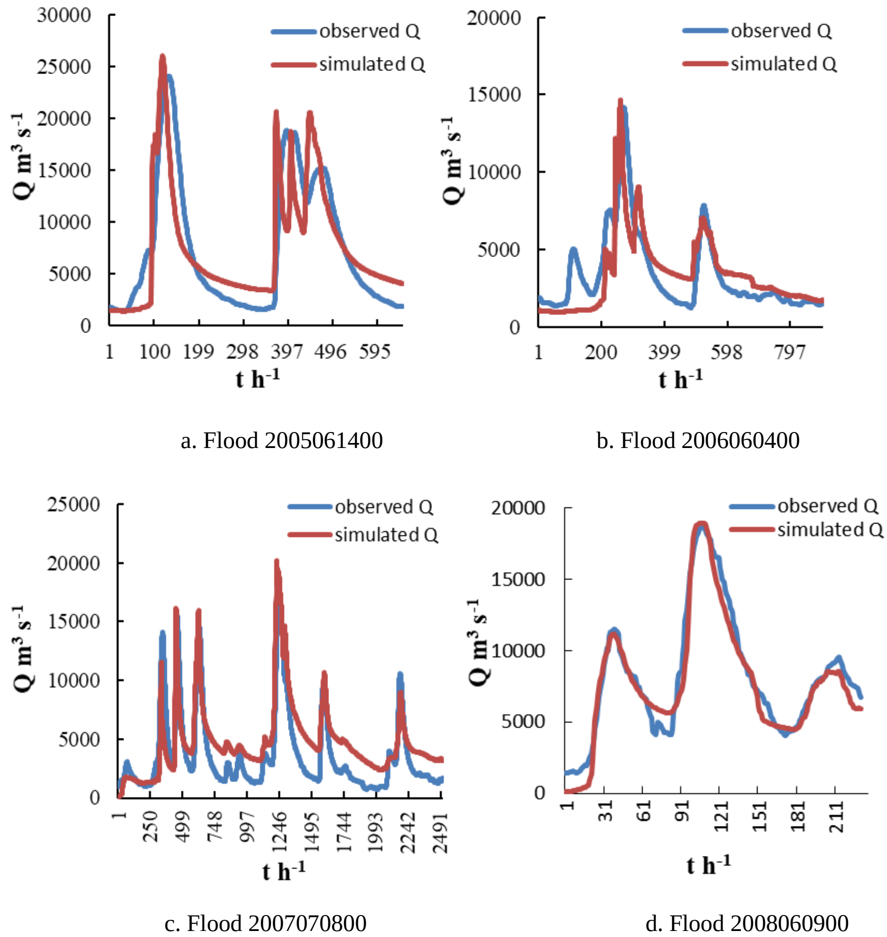

a. Flood 2005061400

b. Flood 2006060400

c. Flood 2007070800

d. Flood 2008060900

Figure 10. The karst floods simulation effects of the coupled model.

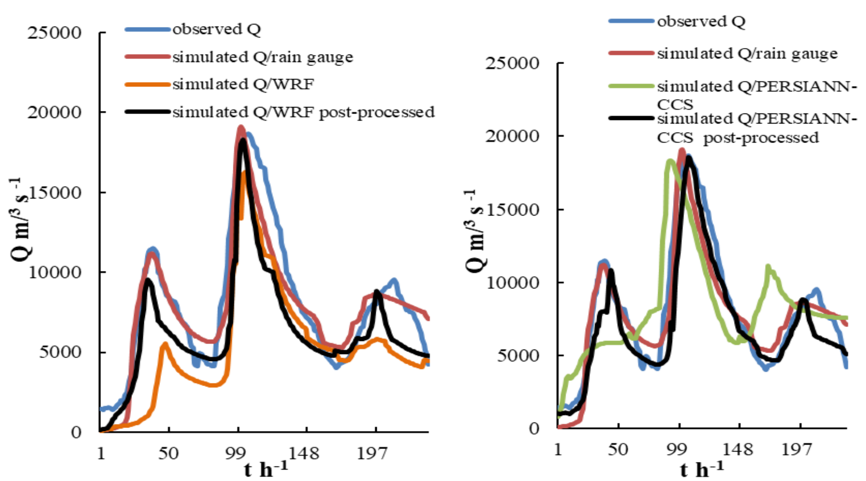

https://doi.org/10.5194/hess-2019-285
Preprint. Discussion started: 8 August 2019

Hydrology and Earth System Sciences
Open Access
Discussions

(a) (b)

Figure 11. The flood simulation results of flood 2008060900 based on the coupled model. (a) is the postprocessed WRF flood simulation result, and (b) is the postprocessed PERSIANN-CCS flood simulation result.

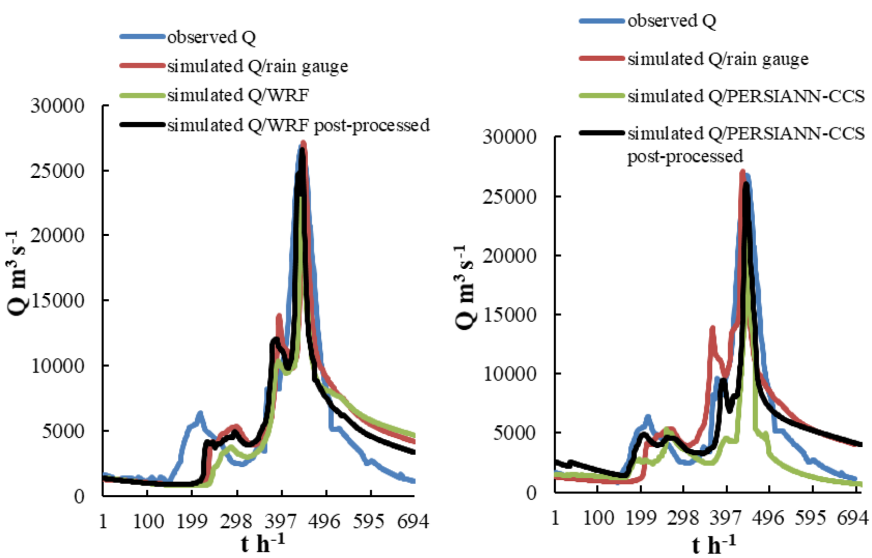

(a) (b)

Figure 12. The flood simulation results of flood 200906090800 based on the coupled model. (a) is the postprocessed WRF flood simulation result, and (b) is the postprocessed PERSIANN-CCS flood simulation result.

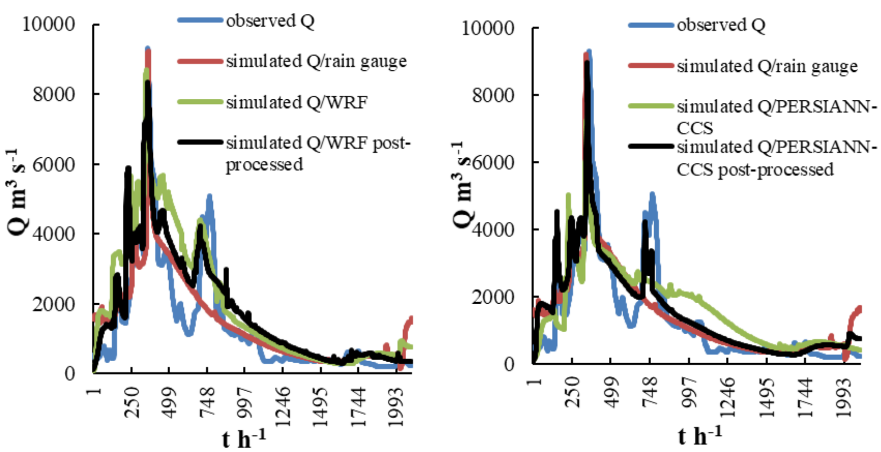

(a) (b)

https://doi.org/10.5194/hess-2019-285
Preprint. Discussion started: 8 August 2019

Hydrology and Earth System Sciences
Open Access
Discussions

Figure 13. The flood simulation results of flood 201106010900 based on the coupled model. (a) is the postprocessed WRF flood simulation result, and (b) is the postprocessed PERSIANN-CCS flood simulation result.

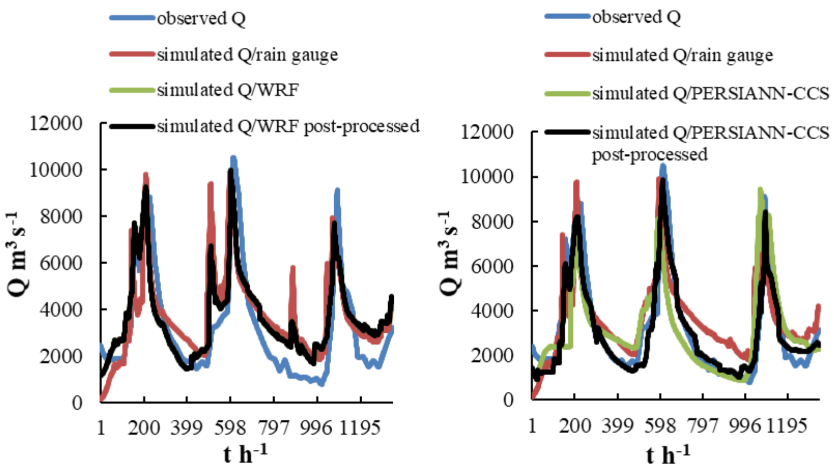

(a) (b)

Figure 14. The flood simulation results of flood 201206022000 based on the coupled model. (a) is the postprocessed WRF flood simulation result, and (b) is the postprocessed PERSIANN-CCS flood simulation result.

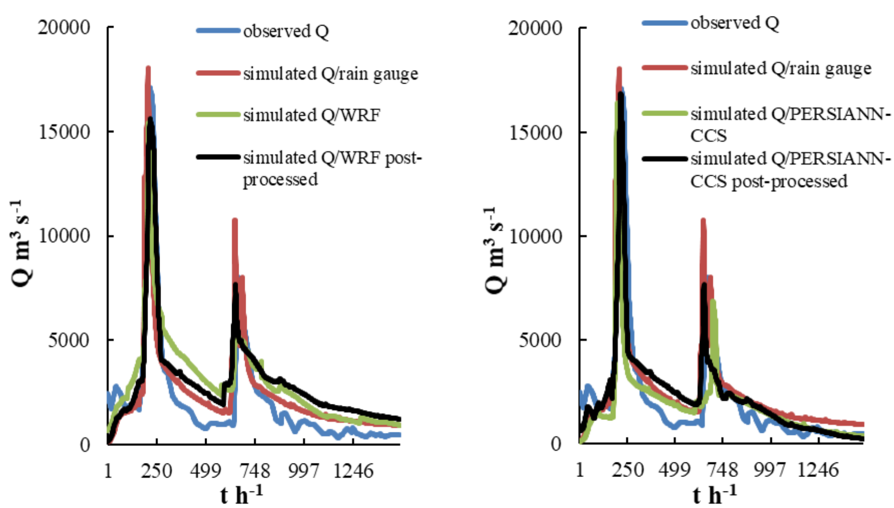

(a) (b)

Figure 15. The flood simulation results of flood 201306011400 based on the coupled model. (a) is the postprocessed WRF flood simulation result, and (b) is the postprocessed PERSIANN-CCS flood simulation result.

https://doi.org/10.5194/hess-2019-285
Preprint. Discussion started: 8 August 2019

Hydrology and Earth System Sciences
Open Access
EGU
Discussions

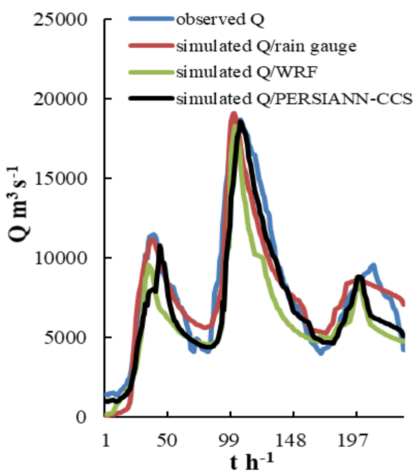

(a) flood 2008060900

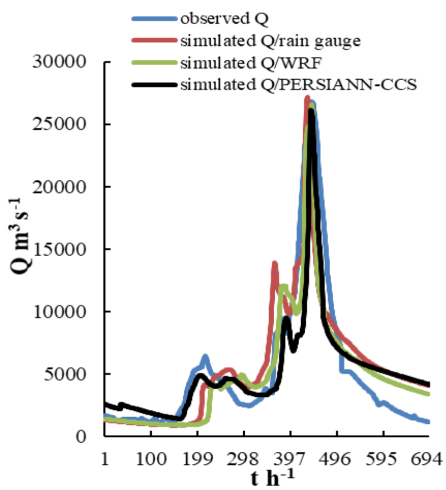

(b) flood 200906090800

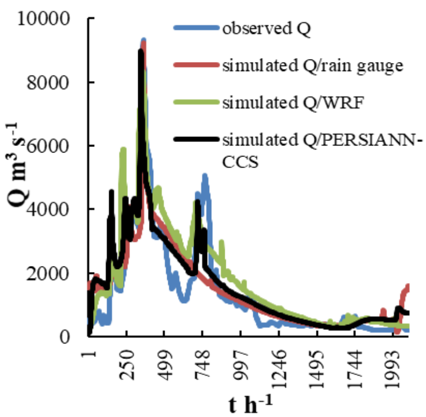

(c) flood 201106010900

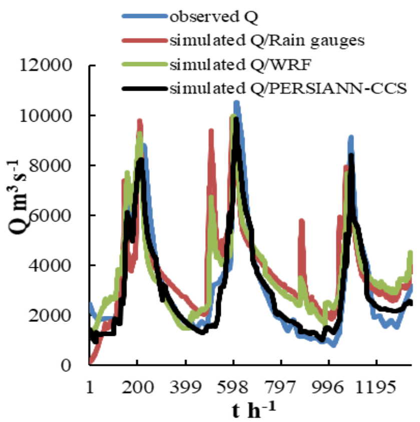

(d) flood 201206022000

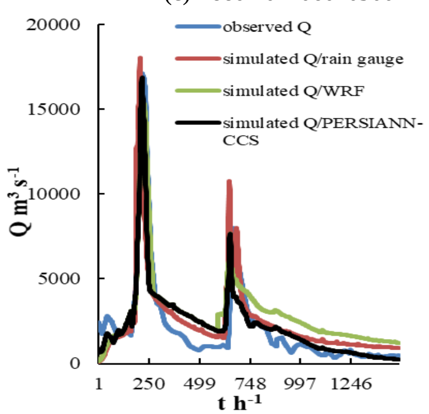

(e) flood 201306011400

Figure 16. The karst floods simulated effects of the coupled model with the 3 precipitation products.

https://doi.org/10.5194/hess-2019-285
Preprint. Discussion started: 8 August 2019

Hydrology and Earth System Sciences
Open Access
Discussions

Tables

Table 1. The quantitative rainfall comparison results of the 3 precipitation products.

Floods	Type	Average precipitation (mm)	Relative bias %
	rain gauge	1.37	
200806090200	WRF QPF	1.55	13
	PERSIANN-CCS QPEs	1.22	-11
	rain gauge	0.74	
200906090800	WRF QPF	0.88	19
	PERSIANN-CCS QPEs	0.62	-16
	rain gauge	0.42	
201106010900	WRF QPF	0.46	10
	PERSIANN-CCS QPEs	0.39	-7
	rain gauge	0.78	
201206022000	WRF QPF	0.95	22
	PERSIANN-CCS QPEs	0.63	-19
	rain gauge	0.53	
201306011400	WRF QPF	0.65	23
	PERSIANN-CCS QPEs	0.43	-20
	rain gauge	0.77	
average value	WRF QPF	0.90	17
	PERSIANN-CCS QPEs	0.66	-14

Table 2. Evaluation indices for the karst floods simulation effects.

Floods	The Nash–Sutcliffe coefficient/C	The correlation coefficient/R	The process relative error/P%	The peak flow relative error/E%	The coefficient of water balance/W	The peak time error/T(hour)
2005061400	0.87	0.92	0.2	0.13	1.08	-7
2006060400	0.91	0.89	0.17	0.07	0.92	-5
2007070800	0.89	0.93	0.14	0.09	1.12	-8
2008060900	0.93	0.95	0.08	0.05	0.94	-3

Table 3. The calculation results of the coupled model parameters sensitivity.

Floods	Potential evaporation/E_p	Evaporation coefficient/λ	Wilting percentage/C_{wl}	The saturated water content/θ_{sat}	The saturation permeability coefficient/θ_s	The macro crack volume ratio/V
	0.05	0.06	0.04	0.9	0.88	0.75
	The field capacity/θ_{fc}	The soil layer thickness/z	The saturated hydraulic conductivity/K_s	The soil coefficient/b	The bottom slope/S_p	The bottom width/S_w
2005061400	0.86	0.67	0.83	0.66	0.36	0.48
	The slope roughness/n	The channel roughness/n_1	The depletion coefficient /ω	The permeability coefficient /K	The specific yield of the aquifer /χ	Thickness of the karst aquifer/h

https://doi.org/10.5194/hess-2019-285
Preprint. Discussion started: 8 August 2019

Hydrology and Earth System Sciences
Discussions

	0.25	0.17	0.13	0.75	0.73	0.68
2006060400	Potential evaporation/E_p	Evaporation coefficient/λ	Wilting percentage/C_{wl}	The saturated water content/θ_{sat}	The saturation permeability coefficient/θ_s	The macro crack volume ratio/V
	0.07	0.13	0.05	0.95	0.91	0.83
	The field capacity/θ_{fc}	The soil layer thickness/z	The saturated hydraulic conductivity/K_s	The soil coefficient/b	The bottom slope/S_p	The bottom width/S_w
	0.9	0.64	0.89	0.6	0.55	0.59
	The slope roughness/n	The channel roughness/n_1	The depletion coefficient /ω	The permeability coefficient /K	The specific yield of the aquifer /χ	Thickness of the karst aquifer/h
	0.3	0.27	0.14	0.75	0.73	0.69
2007070800	Potential evaporation/E_p	Evaporation coefficient/λ	Wilting percentage/C_{wl}	The saturated water content/θ_{sat}	The saturation permeability coefficient/θ_s	The macro crack volume ratio/V
	0.14	0.24	0.08	0.92	0.84	0.75
	The field capacity/θ_{fc}	The soil layer thickness/z	The saturated hydraulic conductivity/K_s	The soil coefficient/b	The bottom slope/S_p	The bottom width/S_w
	0.81	0.63	0.77	0.61	0.51	0.57
	The slope roughness/n	The channel roughness/n_1	The depletion coefficient /ω	The permeability coefficient /K	The specific yield of the aquifer /χ	Thickness of the karst aquifer/h
	0.45	0.4	0.31	0.7	0.69	0.68
2008060900	Potential evaporation/E_p	Evaporation coefficient/λ	Wilting percentage/C_{wl}	The saturated water content/θ_{sat}	The saturation permeability coefficient/θ_s	The macro crack volume ratio/V
	0.18	0.26	0.11	0.94	0.92	0.78
	The field capacity/θ_{fc}	The soil layer thickness/z	The saturated hydraulic conductivity/K_s	The soil coefficient/b	The bottom slope/S_p	The bottom width/S_w
	0.88	0.73	0.82	0.64	0.53	0.6
	The slope roughness/n	The channel roughness/n_1	The depletion coefficient /ω	The permeability coefficient /K	The specific yield of the aquifer /χ	Thickness of the karst aquifer/h
	0.47	0.45	0.36	0.8	0.75	0.72

https://doi.org/10.5194/hess-2019-285
Preprint. Discussion started: 8 August 2019

Hydrology and Earth System Sciences
Open Access
EGU
Discussions

Table 4. The evaluation indices of karst floods simulations with the original WRF QPF and PERSIANN-CCS QPEs and their postprocessed values.

Floods	Types	The Nash–Sutcliffe coefficient/C	The correlation coefficient/R	The process relative error/P%	The peak flow relative error/E%	The coefficient of water balance/W	The peak time error/T(h)
200806090000	WRF QPF	0.72	0.80	25	18	1.02	-9
	The postprocessed WRF QPF	0.78	0.82	20	13	0.95	-7
	PERSIANN-CCS QPEs	0.76	0.83	21	6	0.92	-10
	The postprocessed PERSIANN-CCS QPEs	0.83	0.88	18	5	0.94	-4
200906090800	WRF QPF	0.81	0.82	24	20	1.12	-6
	The postprocessed WRF QPF	0.83	0.83	20	14	1.06	-4
	PERSIANN-CCS QPEs	0.82	0.81	28	18	0.79	-6
	the postprocessed PERSIANN-CCS QPEs	0.85	0.87	22	12	0.85	-3
201106010900	WRF QPF	0.79	0.81	26	14	1.15	-7
	The postprocessed WRF QPF	0.83	0.83	20	10	1.08	-6
	PERSIANN-CCS QPEs	0.85	0.85	21	12	0.92	-8
	The postprocessed PERSIANN-CCS QPEs	0.91	0.87	19	6	0.94	-6
20120602200	WRF QPF	0.78	0.82	18	13	1.28	-10
	The postprocessed WRF QPF	0.81	0.83	10	11	1.15	-8
	PERSIANN-CCS QPEs	0.86	0.84	16	15	0.78	-7
	the postprocessed PERSIANN-CCS QPEs	0.92	0.89	9	6	0.85	-4
201306011400	WRF QPF	0.78	0.82	13	21	1.20	-8
	The postprocessed WRF QPF	0.82	0.85	9	12	1.12	-6

	PERSIANN-CCS QPEs	0.82	0.89	12	17	0.85	-5
	The postprocessed PERSIANN-CCS QPEs	0.86	0.91	8	9	0.87	-4
average value	WRF QPF	0.78	0.81	21	17	1.15	-8
	The postprocessed WRF QPF	0.81	0.83	16	12	1.07	-6
	PERSIANN-CCS QPEs	0.82	0.84	20	14	0.85	-7
	The postprocessed PERSIANN-CCS QPEs	0.87	0.88	15	8	0.89	-4

Table 5. The evaluation indices of karst floods simulations with the 3 precipitation products.

Floods	Type	Nash–Sutcliffe coefficient/C	Correlation coefficient/R	Process relative error/P%	Peak flow relative error/E%	The coefficient of water balance/W	Peak time error/T (hour)
200806090000	rain gauge	0.85	0.91	15	3	0.89	-6
	WRF QPF	0.78	0.82	20	13	0.95	-7
	PERSIANN-CCS QPEs	0.83	0.88	18	5	0.94	-4
200906090800	rain gauge	0.95	0.92	17	4	0.9	-2
	WRF QPF	0.83	0.83	20	14	1.06	-4
	PERSIANN-CCS QPEs	0.85	0.87	22	12	0.85	-3
201106010900	rain gauge	0.95	0.92	16	3	1.02	-7
	WRF QPF	0.83	0.83	20	10	1.08	-6
	PERSIANN-CCS QPEs	0.91	0.87	19	6	0.94	-6
20120602200	rain gauge	0.93	0.91	8	5	0.89	-6
	WRF QPF	0.81	0.83	10	11	1.15	-8
	PERSIANN-CCS QPEs	0.92	0.89	9	6	0.85	-4
201306011400	rain gauge	0.95	0.94	7	6	0.92	-4
	WRF QPF	0.82	0.85	9	12	1.12	-6
	PERSIANN-CCS QPEs	0.86	0.91	8	9	0.87	-4
average value	rain gauge	0.93	0.92	13	4	0.92	-5
	WRF QPF	0.81	0.83	16	12	1.07	-6
	PERSIANN-CCS QPEs	0.87	0.88	15	8	0.89	-4

References

Ahlgrimm, M., Forbes, R. M., Morcrette, J.J., and Neggers, R. A.: ARM's Impact on Numerical Weather Prediction at ECMWF, Meteorol. Monogr., 57, 28.1–28.13, 2016.

Ambroise, B., Beven, K., and Freer, J.: Toward a generalization of the TOPMODEL concepts: Topographic indices of hydrologic similarity, Water Resour. Res., 32, 2135–2145, 1996.

Atkinson, T. C.: Diffuse flow and conduit flow in limestone terrain in the Mendip Hills, Somerset, Great Britain, J. Hydrol., 35, 93–110, 1977.

Bartsotas, N., Nikolopoulos, E., Anagnostou, E., and Kallos, G.: Improving satellite quantitative precipitation estimates through the use of high-resolution numerical weather predictions: Similarities and contrasts between the Alps and Blue Nile region, EGU General Assembly Conference Abstracts, 19th EGU General Assembly, EGU 2017, 23–28 April, p. 9673, Vienna, Austria,2017.

Chen, Y. B.: Liuxihe Model, China Science and Technology Press, Peking, China, 2009.

Chen, Y., Li, J., and Xu, H.: Improving flood forecasting capability of physically based distributed hydrological models by parameter optimization, Hydrol. Earth Syst. Sci., 20, 375–392, https://doi.org/10.5194/hess-20-375-2016, 2016.

Chen, Y., Li, J., Wang, H., Qin, J., and Dong, L.: Large watershed flood forecasting with high-resolution distributed hydrological model, Hydrol. Earth Syst. Sci., 21, 735–749, https://doi.org/10.5194/hess-21-735-2017, 2017.

Chen, Y.: Distributed Hydrological Models. Springer Berlin Heidelberg, Switzerland, https://doi.org/10.1007/978-3-642-40457-3_23-1,2018.

Choi, J., Harvey, J.W., and Conklin, M. H.: Use of multi-parameter sensitivity analysis to determine relative importance of factors influencing natural attenuation of mining contaminants, The Toxic Substances Hydrology Program Meeting, Charleston, South Carolina,1999.

Chou, M. D. and Suarez, M. J.: An efficient thermal infrared radiation parameterization for use in general circulation models, NASA Tech. Memo 104606, NASA, 1–92, 1994.

Delrieu, G., Bonnifait, L., Kirstetter, P. E., and Boudevillain, B.: Dependence of radar quantitative precipitation estimation error on the rain intensity in the Cévennes region, France, Hydrolog. Sci. J., 59, 1308–1319, 2014.

Ek, M. B., Mitchell, K. E., Lin, Y., Rogers, E., Grunmann, P., Koren, V., Gayno, G., and Tarpley, J. D.: Implementation of Noah land surface model advances in the National Centers for Environmental Prediction operational mesoscale Eta model, J. Geophys. Res., Atmos., 108, 1–16, 2003.

Fan, K. K., Duan, L. M., Zhang, Q., Shi, P. J., Liu, J. Y., Gu, X.H., and Kong, D. D.: Downscaling Analysis of TRMM Precipitation Based on Multiple High-resolution Satellite Data in the Inner Mongolia, China, Scientia Geographica Sinica, 37, 1411–1421, 2017.

Fan, Z., Hao, Z., Chen, Y., Wang, J.H., and Huang, F.H.: The Application and Research of Income Flood Simulation of the Baipenzhu Reservoir with the Liuxihe Model. Acta Scientiarum Naturalium Universitatis Sunyatseni, 51(2):113-118, 2012.

Faure, D., Gaussiat, N., Tabary, P., and Urban, B.: Real time integration of foreign radar quantitative

https://doi.org/10.5194/hess-2019-285
Preprint. Discussion started: 8 August 2019

precipitation estimations (QPEs) in the French national QPE mosaic, Conference on Radar Meteorology, AMS, Marseilles, France, 21–21, 2015.

Ford, D. and Williams, P. W.: Karst Geomorphology and Hydrology, Unwin Hyman, London, 1989.

Gallegos, J.J., Hu, B.X., Davis, H.: Simulating flow in karst aquifers at laboratory and sub-regional scales using MODFLOW-CFP. Hydrogeology journal, 21(8): 1749-1760, 2013.

Ghasemizadeh, R., Hellweger, F., Butscher, C., Padilla, I., Vesper, D., Field, M., and Alshawabkeh, A.: Review: Groundwater flow and transport modeling of karst aquifers with particular reference to the North Coast Limestone aquifer system of Puerto Rico. HvdroQeologv Journal, 20(8): 1441-1461, 2012.

Goldscheider, N. and Drew, D.: Methods in Karst Hydrogeology: IAH: International Contributions to Hydrogeology, 26, CRC Press, The University of Auckland, New Zealand, 2007.

Goudenhoofdt, E. and Delobbe, L.: Evaluation of radar-gauge merging methods for quantitative precipitation estimates, Hydrol. Earth Syst. Sci., 13, 195–203, https://doi.org/10.5194/hess-13-195-2009, 2009.

Han, D.W., Kwong, T., and Li, S.: Uncertainties in real-time flood forecasting with neural networks, Hydrol. Process., 21, 223–228,2007.

Hartmann, A., Barberá, J. A., Lange, J., Andreo, B., and Weiler, M.: Progress in the hydrologic simulation of time variant recharge areas of karst systems – Exemplified at a karst spring in Southern Spain, Adv. Water Resour., 54, 149–160, 2013.

Hong, S. and Lim, J.: The WRF Single-Moment 6-Class Microphysics Scheme (WSM6), J. Korean Meteorol. Soc., 42, 129–151, 2006.

Hu, Q. F., Yang, D.W., Wang, Y. T., Yang, H. B., and Liu, Y.: Characteristics and sources of errors in daily TRMM precipitation product over Ganjiang River basin in China, Adv. Water Sci.,24, 794–800, 2013.

Hui, Z., Chen, Y., and Zhou, J.H.: Assessing the long-term impact of urbanization on run-off using a remote-sensing-supported hydrological model. International Journal of Remote Sensing, 36(21):1-17, 2015.

Kain, J. S.: The Kain–Fritsch convective parameterization: An update, J. Appl. Meteorol. Clim., 43, 170–181, 2004.

Kovacs, A. and Perrochet, P.: Hydrograph Analysis for Parameter Estimation of Connected and Karst Systems, Proceedings of the 34th World Congress of the International Association for Hydro-Environment Research and Engineering: 33rd Hydrology and Water Resources Symposium and 10th Conference on Hydraulics in Water Engineering, Engineers Australia, 1627–1634, Neuchatel, Switzerland, 2011.

Li, J., Chen, Y., Wang, H., Qin, J., Li, J., and Chiao, S.: Extending flood forecasting lead time in a large watershed by coupling WRF QPF with a distributed hydrological model, Hydrol. Earth Syst. Sci., 21, 1279–1294, https://doi.org/10.5194/hess-21-1279-2017,2017.

Li, J., Yuan, D., Liu, J., Jiang, Y., Chen, Y., Hsu, K. L., and Sorooshian, S.: Predicting floods in a large karst river basin by coupling PERSIANN-CCS QPEs with a physically based distributed hydrological model, Hydrol. Earth Syst. Sci., 23, 1505-1532, https://doi.org/10.5194/hess-23-1505-2019, 2019.

Li, Y., Lu, G. H., Wu, Z. Y., and Shi, J.: Study of a dynamic downscaling scheme for quantitative precipitation forecasting, Remote Sensing and GIS for Hydrology and Water Resources, Proc. IAHS, 368, 108–113, doi:10.5194/piahs-368-108-2015, 2015.

Liao, Z., Chen, Y., Xu, H.J., Yan, W.L., and Ren, Q.W.: Parameter Sensitivity Analysis of the Liuxihe Model Based on E-FAST Algorithm. Tropical Geography, 32(6):606-612,632, 2012.

Mlawer, E. J., Taubman, S. J., Brown, P. D., Iacono, M. J., and Clough, S. A.: Radiative transfer for inhomogeneous atmospheres: RRTM, a validated correlated-k model for the longwave, J. Geophys. Res.-Atmos., 102, 16663–16682, doi: 10.1029/97JD00237, 1997.

Molteni, F., Buizza, R., Palmer, T. N., and Petroliagi, T.: The ECMWF Ensemble Prediction System: Methodology and validation, Q. J. Roy. Meteorol. Soc., 122, 73–119, 1996.

Quinlan, J. F., and Ewers, R. O.: Ground water flow in limestone terranes – strategy, rationale and procedure for reliable, efficient monitoring of ground water in karst areas, Mendeley, 8, 167–173, 1985.

Rafieei, N. A., Norouzi, A., Kim, B., and Seo, D.: J Fusion of multiple radar-based quantitative precipitation estimates (QPE) for high-resolution flash flood prediction in large urban areas, AGU Fall Meeting Abstracts, AGU Fall Meeting, San Francisco, CA, USA, 2014.

Scanlon, B.R., Mace, R.E., Barren, M.E., and Smith, B.: Can we simulate regional groundwater flow in a karst system using equivalent porous media models? Case study, Barton Springs Edwards aquifer, USA. Journal of Hydrology, 276(1-4): 137-158, 2003.

Skamarock, W. C., Klemp J. B., Dudhia, J., Gill, D. O., Barker,D. M., Duda, G., Huang, X., Wang, W., and Powers, J. G.: A Description of the Advanced Research WRF Version 3, NCAR Technical Note, NCAR/TN-468, STR, National Center For Atmospheric Research, Boulder, CO, Mesoscale and Microscale Meteorology Div., Denver, Colorado, USA, 2008.

Stenz, R. D.: Improving satellite quantitative precipitation estimates by incorporating deep convective cloud optical depth, Dissertations & Theses – Gradworks, The University of North Dakota,USA, 2014.

Takenaka, H., Nakajima, T. Y., Higurashi, A., Higuchi, A., Takamura,T., Pinker, R. T., and Nakajima, T.: Estimation of solar radiation using a neural network based on radiative transfer, J. Geophys. Res., 116, D08215, doi:10.1029/2009JD013337, 2011.

Tingsanchali, T.: Urban flood disaster management, Procedia Eng., 32, 25–37, 2012.

Wardhana, A., Pawitan, H., and Dasanto, B. D.: Application of hourly radar-gauge merging method for quantitative precipitation estimates, in: IOP Conference Series: Earth and Environmental Science, Vol. 58, No. 1, p. 012033, IOP Publishing, https://doi.org/10.1088/1755-1315/58/1/012033, 2017.

White, W.B.: Karst hydrology: recent developments and open questions. Engineering geology, 65(2-3): 85-105, 2002.

White, W.B., White, E. L.: Ground water flux distribution between matrix, fractures, and conduits: constraints on modeling. Speleogenesis and evolution of Karst aquifers, 3(2): 1-6, 2005.

White, W.B.: A brief history of karst hydrogeology: contributions of the NSS. Journal of Cave and Karst Studies, 69(1): 13-26, 2007.

Yang, H., Gochis, D., Cheng, J. T., Hsu, K. L., and Soroosh, S.: Evaluation of PERSIANN-CCS Rainfall Measurement Using the NAME Event Rain Gauge Network, J. Hydromteorol., 8, 469–482, 2007.

Yang, H., Hsu, K. L., Soroosh, S., and Gao, X. G.: Precipitation Estimation from Remotely Sensed Imagery Using an Artificial Neural Network Cloud Classification System, J. Appl. Meteorol., 36, 1176–1190, 2004.

Zappa, M., Beven, K. J., Bruen, M., Cofino, A. S., Kok, E. M.,Nurmi, P., Orfila, B., Roulin, E., Schroter, K., Seed, A., Szturc, J., Vehvilainen, B., Germann, U., and Rossa, A.: Propagation of Uncertainty from observing systems and NWP into hydrological models: COST-731 Working Group 2, Atmos. Sci. Lett., 11, 83–91, 2010.